United through separation - a study of the coalescence behaviour of separating micro-droplets

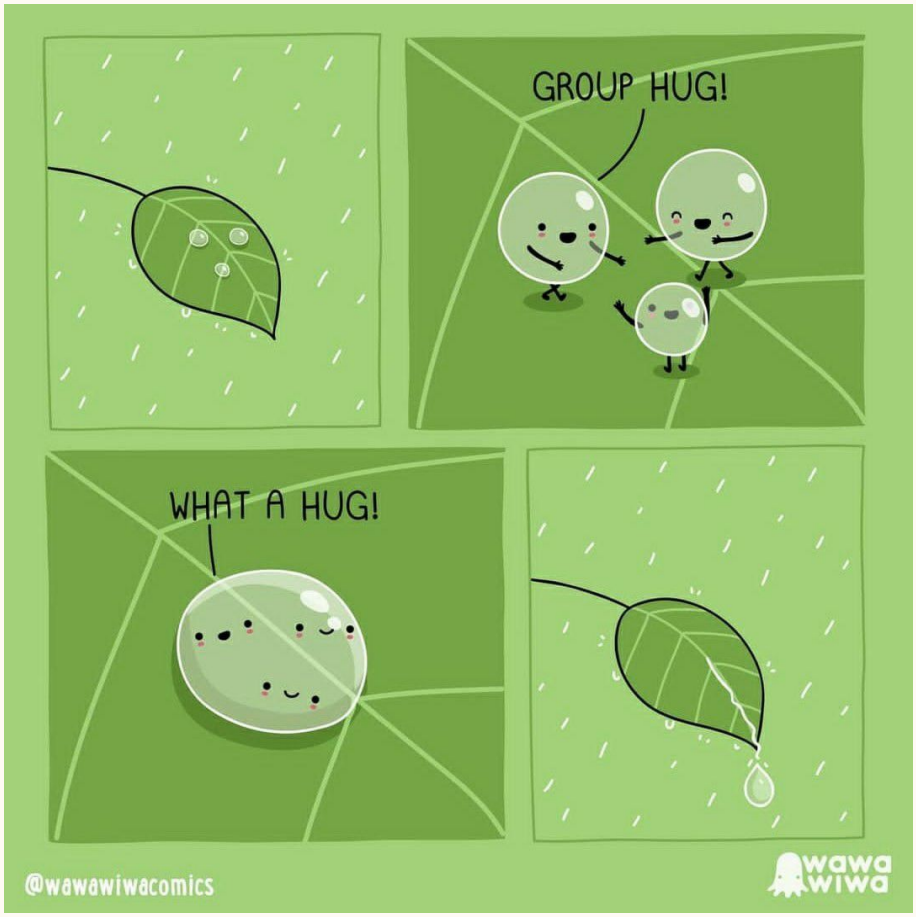

Author:
Sowmya Kumar

Supervisors
Prof. dr. ir. Jerry Westerweel
Dr. Daniel Tam

Daily Supervisor
Dr. Teng Dong

United through separation - a study of the coalescence behaviour of separating micro-droplets

by

Sowmya Kumar

to obtain the degree of Master of Science
at the Delft University of Technology,
to be defended publicly on Thursday September 30, 2021.

Student number:	5061989	
Project duration:	Dec 1, 2020 – September 30, 2021	
Thesis committee:	Prof. dr. ir. J. Westerweel,	TU Delft, supervisor
	Dr. D. Tam,	TU Delft, supervisor
	Dr. H. Bazyar,	TU Delft, committee member
	Dr. T. Dong ,	TU Delft, daily supervisor

This thesis is confidential and cannot be made public until September 30, 2021.

TU Delft

Preface

If there is one part of writing this report that I have contemplated about arguably more than the rest, it would be this single page. It is the single sheet of paper, brimming with honesty, that can render an even-handed perspective to the rest of this document that is otherwise so seamlessly woven (at least in attempt) into a coherent story, shelving away the confusions, errors and mistakes that plagued my life during the nine months that this story spans. To these lovely nine months, to the people and the events that made it so, I owe this moment of unabashed honesty.

As a child, I was an ardent Monday-hater. Not just any Monday-hater, but the few who very literally shed a couple of tears while lying in bed, contemplating the horrors entailing another five days in school. When I grew up, my tears gave way to a sense of forlorn that I resigned to carrying along with me as I showed up to the beginning of the week. But to my surprise and joy, I have treated the Mondays in the past year with almost no ounce of dread. It seems strange - how being seated at the edge of my chair peering through the microscope can make a difference, but a whole new world existed through that lens - a world I had only heard of in lecture halls and tried hard to imagine. Least to say, Mondays were met with equal tranquility as Fridays. Having achieved the unfathomable, I have enough evidence to say that now, my lens has changed and I like this chair.

Many small battles were fought in the last two years at TU Delft, and the trickiest one was becoming comfortable with addressing my teachers by their first names. Teachers have made and broken me. Some teachers from childhood set off insecurities that I hold unto this day. But there were others who sparked my interest, in whose classes I realized the joy of learning and was humbled through the boundless exercise of re-learning. I want to take this opportunity to express my gratitude to my teachers whose contagious love for their field has been instrumental in keeping my spirit alive. I can never repay any of you and I shall never attempt to.

In this vein, I extend my deepest gratitude to my thesis supervisors- my first window into the world of scientific research- **Prof.dr.ir. Jerry Westerweel**, who taught me the power of intelligent first estimates in research, and **Dr. Daniel Tam** whose palpable passion for fluid dynamics, evident in his lectures, marked the beginning of my journey in the field. With more pride than shame, I admit to have known astonishingly little at the beginning of AFD. I could not have enjoyed working on this thesis without the support of **Dr. Teng Dong**, whose words of encouragement helped me through disappointing times. Thank you for never dismissing any of my ideas, however impractical, and for being a reminder that learning can never stop.

I would like to mention my friends in Delft, **Sahiti**, **Uma** and **Aarthi**- without whose love, genuineness and company, TU Delft may have remained challenging, but not a learning experience. You girls were my family here. I would also like to thank all my friends- from my childhood up to now - who fascinate me with their minds and strengthen me through their kindness. I thank my parents, **Amma** and **Appa**, for their unwavering support and love. If not for the both of you, I would never have made it this far (also, quite literally).

The best decisions I have made in life were never made alone. In moments of anxiety and confusion, it has always been you, **Divya**, who has resounded reason and logic. It is unimaginable, to me, who I would have become without you. Everything I am today, all the good and bad, my identity and my values – I owe it all to you. You are my soul-sister. At the end of these two magical years at TU Delft, I have with me, this 50 page document, the single piece of work I am undoubtedly proudest of - a testament to my beliefs, my insecurities, my fears and my goodness. I dedicate this to you, not in a manner of contented resignation but, knowing that looking back at this period in my life, that I consider the best version of myself, you will remind me to strive for the 'better' that lies beyond the best.

ll Vande Guru Paramparam ll
(Salutations to my lineage of teachers)

- Sowmya Kumar
Delft, 2021

"All the good is an imposter",
said the little monster.
"Your trips, your falls, the scar,
is who you truly are!"

"There are no other but two kind,
The best and the ones behind.
You slip, you fall, your scar
We see which kind you are!"

"So you slip, but when you fall
Cover your tracks, hide them all.
Fear and to that pray
In moments that count, your imposter stays."

"If there were no more but two kind,
what about our limitless mind?
Born alike, built by chance
out of experiences and circumstance."

"My trips, my falls, my scars
signs that I have come far.
If in this world it costs to try
isn't it how our spirits die?"

Contents

List of Figures

List of Tables

Abstract

The coalescence of two droplets suspended in a viscous fluid is the focus of this study. When two droplets that are suspended in a shearing flow come in contact with each other, it is currently uncertain if the contact would result in coalescence. To be able to make such predictions, it is necessary to systematically study the effects of the system parameters, such as the angle of collision between the droplets and the properties of the flow and the two fluids, on the process of coalescence. This necessitates the need for a robust experimental setup in which such studies can be performed.

The characteristic of a systematic study is repeatability and control over experimental conditions. In coalescence studies, the impact angle between the droplets is a parameter that has proved difficult to control. In this study, a microfluidic device is developed that uses the concept of surface energy wells to achieve repeatability in the impact angles of droplet collisions. Using the device, droplet coalescence experiments were performed. An interesting observation was made from the experiments which guided the further course of this research work. It was seen that the droplets did not coalesce upon approach, but coalescence was driven by the separation of the droplets. In the literature, this phenomenon is referred to as 'separation-driven coalescence'. Furthermore, it was suspected that an experimental condition could be defined based on a non-dimensional parameter, namely the Capillary number Ca, such that for $Ca > Ca_{\mathrm{cr}}$, separation of droplets ceases to trigger coalescence.

The effect of the system parameters, namely the impact angle, θ_{i}, and the viscosity ratio, λ, over the Ca_{cr} was investigated. In this study, the presence of a Ca_{cr} for separation-driven coalescence is confirmed, both experimentally and through the development of a scaling model. The results of the study indicate that the thickness of the film on the onset of separation influences the Ca_{cr}. However, a dependency between the Ca_{cr} and λ was not found experimentally. Large experimental uncertainties prevent any further conclusions to be made regarding the Ca_{cr}.

In this thesis, a framework is developed for the investigation of Ca_{cr} for separation-driven coalescence. With more experimental data, a deeper understanding of separation-driven coalescence can be obtained.

Keywords - *droplet coalescence, shear, microfluidics, surface energy wells, separation-driven coalescence*

1

Motivations

Coalescence is the process of two (or more) droplets or bubbles forming one single droplet or bubble. In a multi-phase flow, coalescence may be facilitated by different forces such as gravity forces, turbulent forces, or inertial forces (Kamp et al., 2017). In this thesis, we are interested in the coalescence of droplets in shearing flows. It is an interesting problem primarily because not all is understood about this fascinating phenomenon. While scientific curiosity is certainly a motivation for this research, other research problems also benefit from this study namely- droplet-based microfluidics and stability of industrial emulsion systems. In this section, we elaborate on our motivations for this study.

1.1. Droplet-based microfluidics

Droplet-based microfluidics has become an evolving platform for the development of sophisticated research tools in the fields of chemistry and biology (Theberge et al., 2010). There are several reasons for the growing interest in this field amongst the scientific community. Firstly, molecules, chemical reagents, and particles including microorganisms can be isolated and compartmentalized within droplets (Lederberg, 1954). Along with compartmentalization of materials, the homogeneous conditions within a droplet, the high surface-to-volume ratio of droplets, and internal circulation within droplets make them ideal chemical reactors (Joanicot and Ajdari, 2005). Secondly, droplet generation in microfluidic devices can be fast and precise (Link et al., 2004). It is possible to control the size of each droplet generated in a microfluidic device. Mono-disperse and polydisperse emulsions were created by integrating a 'flow-focussing' geometry in microfluidic channels (Anna et al., 2003). The identical nature of successive droplets makes droplet-based microfluidic devices suitable for quantitative studies (Theberge et al., 2010). Additionally, femto-nanolitre size droplets are generated in microfluidic channels (Joanicot and Ajdari, 2005, Theberge et al., 2010). Using such devices for screening and analysis of compounds allows us to use small amounts of reagents. This is an attractive feature for drug discovery, gene testing, and other biological research applications where only small amounts of reagents may be required for screening but reagents (for example, enzymes) are rare and expensive (Theberge et al., 2010).

Despite such attractive features, the field of droplet-based microfluidics is still in its infancy. Several bottlenecks are identified in the current state-of-the-art of microfluidic devices. Droplet production is

not mono-disperse until the system pressures become stable (Theberge et al., 2010). This can lead to the wastage of precious reagents during the start-up of the droplet generation process in microfluidic devices. Unwarranted coalescence and breakup of droplets can occur in microfluidic devices necessitating the use of surfactants (Anna et al., 2003). While using droplets as chemical reactors, we need to ensure that the residence time of the droplets within microfluidic devices is sufficient in the context of the kinetics of the reaction. These require additional features such as droplet traps (Shim et al., 2007) or delay lines in the channels (Frenz et al., 2009). The selected challenges discussed here already reveal that the design and fabrication of every microfluidic device require customization in design and/or operation to promote certain features and discourage others. It is important to note here that the choices we make, as developers, in the design of microfluidic devices will dictate the versatility of their use.

For microfluidics to become successful, it needs to become commercial- it should not remain to be a field limited to academic papers (Whitesides, 2006). It should be able to serve users who are not necessarily experts in the field. This relies on our ability to design and fabricate robust microfluidic devices. The robustness of the device can be attributed to the repeatability and control over some basic functions such as droplet generation, splitting, sorting, trapping, and coalescence. For example, droplet generation is currently controlled by changing the input flow rates of the two phases. However, this simultaneously affects the droplet size, the frequency of generation, and the speed of the droplet, all of which may not be desired (Joanicot and Ajdari, 2005). On-chip control may be achieved by incorporating active systems in the device such as actuators, but it comes at the cost of increasing the complexity of the design and limiting the flexibility over the applications of the device. Adding active elements into the design also complicates the fabrication of the device (Theberge et al., 2010). It is, therefore, worthy to focus on the standardization of the basic functions with an intentional drift towards passive designs based on the geometry of the channel and wall effects (Joanicot and Ajdari, 2005). In this study, we focus on standardizing the coalescence process in a microfluidic device through a design based on passive elements.

1.2. Dispersion systems in industrial processes

A disperse system is a two-phase system in which an immiscible dispersed phase (solid particle or liquid droplets) is distributed through a continuous phase (Brunaugh et al., 2019). An emulsion, such as milk and mayonnaise, cosmetic products like creams and lotions, is an example of a dispersion system. A polymer blend is an emulsion system that combines desirable properties of different polymers into one single heterogeneous material or product. The drop size distribution of the polymer blend determines the characteristics of the product. It is, therefore, important to control the drop size distribution of the emulsion in the process of creating the blend.

The process of creating emulsions is called emulsification. Shearing flows are used in current industrial techniques for the emulsification process (Leal-Calderon et al., 2007). In shearing flows, changes to drop-size distribution are due to two main processes- splitting and coalescence (Vinckier et al., 1998). Depending on the volume ratio and viscosity ratio of the two phases, the coalescence of droplets can lead to the destruction of the emulsion system (Meleson et al., 2004). It is, therefore, necessary to determine the operating conditions under which the desired drop size distribution is achieved and optimal characteristics of the emulsion/blend is obtained. To this, we need to understand the effect of the system parameters on the breakup and coalescence of droplets.

2

Background

Coalescence is driven by the minimization of interfacial energy (Kamp et al., 2017) - after two droplets coalesce, the resulting droplet has a lower interfacial area than the sum of the interfacial areas of the two initial droplets. Reduction of the interfacial area is favored because when an interface is formed, the unbalanced intermolecular forces experienced by the molecules at the interface give rise to free energy to molecules at the interface. As a result, it costs energy for a system to have an interface and any system tries to minimize its interfacial area.

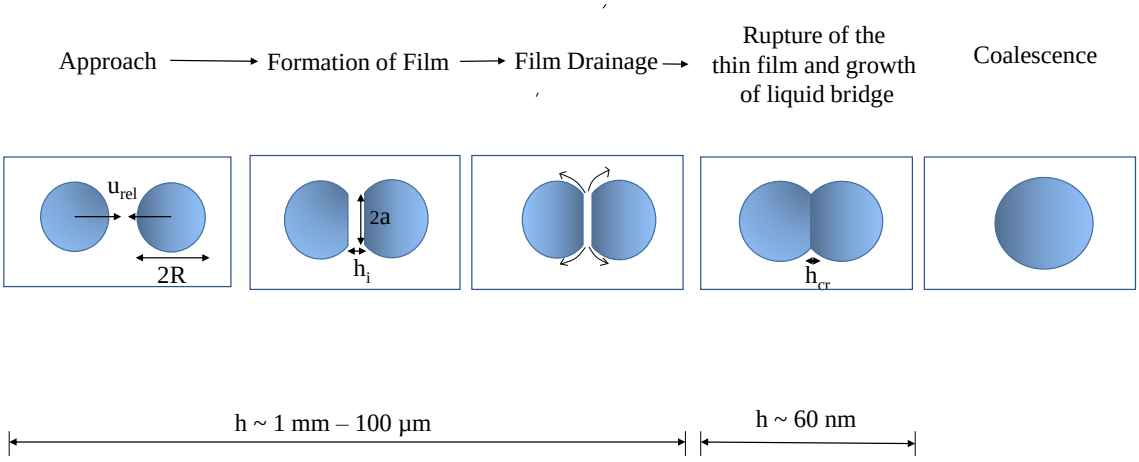

Figure 2.1: A schematic of the several processes constituting the coalescence of two droplets. In this illustration, we have assumed the shape of the film to be disk-shaped.

Coalescence involves complex interactions between the droplets, referred to as the dispersed phase, and the fluid in which the droplets are suspended, referred to as the continuous phase (Chesters, 1991). A way to tackle this complexity is to break the process into many individual coupled processes. Figure 2.1 represents the many sub-processes that together constitute the process of coalescence. Two droplets collide due to a relative velocity between them. The relative velocity between the droplets depends on the flow regime of the two-phase flow and the buoyancy of the droplets in the continuous phase (Kamp et al., 2017). As the droplets approach closer to each other, the pressure of the continuous phase in the region between the two droplets increases. The higher pressure in this region compared

to the pressure of the continuous phase far away drives the flow of the continuous phase out of this region. Simultaneously, since the droplet interfaces are deformable, the increase in the pressure of the continuous phase in the region between the droplets causes the droplet interfaces to deform. We assume that the interfaces deform in such a manner that they form two parallel disks facing each other, enclosing a thin film of the continuous phase of radius, a. The initial thickness of the thin film, h_{i}, is much smaller compared to the radius of the film, a. The thickness of the film decreases with time due to the drainage of the film. The drainage of the thin film is the rate-limiting step of the drainage process (Chesters, 1991). For pure liquids, when the film has thinned to a thickness of h_{cr}, Van der Waals forces become dominant over the viscous and interfacial forces and the film ruptures. Rupture of the film leads to the formation of a liquid bridge of the dispersed phase that connects the two droplets. The growth of this liquid bridge leads to the formation of the coalesced droplet (Janssen and Anderson, 2011).

Despite such attempts made to simplify the process of coalescence, it is still a challenging phenomenon to study. The length scales and time scales governing the sub-processes can be several orders of magnitude apart (see figure 2.1). To illustrate this point, the critical rupture thickness is of the order of 60 nm while film drainage occurs over a length scale of 100 μm to 1 mm (Janssen and Anderson, 2011). Similarly, the growth of the liquid bridge for aqueous water droplets occurs over a time scale of 10^{-10} s (Aarts et al., 2005) while a typical film drainage time is of the order of 10^{-3} s (Kamp et al., 2017). Furthermore, the processes are heavily coupled and complex interactions exist on and across all the scales (Kamp et al., 2017). Therefore, it is difficult for a single study, experimental or numerical, to resolve all the scales involved in the process. In this study, we will focus on processes that occur at length scales of the order of 100 μm- 1 mm and time scales of the order of $10^{-4} - 10^{-3}$ s.

This chapter provides the required background knowledge for the work presented in this thesis. First, we define the problem, in physical terms, by performing a dimensionless analysis. Then, a commonly used scaling model for estimating the drainage rates of the film, referred to as the parallel-disk model, is presented. An overview of the experimental studies is given and the results from the studies are compared against the prediction of the parallel-disk model. Following this, the objectives of this thesis is discussed.

Dimensionless groups

The collision of two neutrally buoyant droplets in a shear-dominated flow regime can be described by six parameters namely, the viscosity of the continuous phase μ_{c}, the viscosity of the dispersed phase μ_{d}, the relative velocity of the droplets u_{rel}, the radius of the droplets R ,the interfacial tension σ and the offset distance, l (see figure 2.3). In this thesis, we study the two-phase flow of neutrally buoyant droplets in a viscous fluid. Inertial and gravity forces are assumed to be less important when compared to viscous forces. Therefore, $u_{\mathrm{rel}} \sim \dot{\gamma} R$ where $\dot{\gamma}$ is the strain rate in the flow field. According to the Buckingham pi theorem, three dimensionless groups govern the collision process namely the viscosity ratio $\lambda = \frac{\mu_{\mathrm{d}}}{\mu_{\mathrm{c}}}$,the offset ratio, $\Delta = \frac{l}{d}$ and the Capillary number, $Ca = \frac{\mu_{\mathrm{c}} u_{\mathrm{rel}}}{\sigma} = \frac{\mu_{\mathrm{c}} \dot{\gamma} R}{\sigma}$. The Ca characterizes the problem since we expect the outcome of the collision to be governed by viscous forces and interfacial forces.

1. Viscosity ratio, λ

The viscosity ratio influences the mobility of the interface. When λ tends to infinity, the viscosity of the

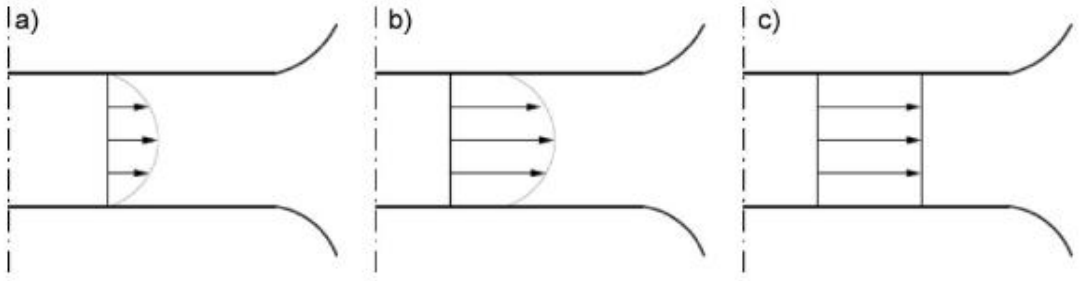

Figure 2.2: The schematic represents the velocity profiles in the thin film depending on the mobility of the interface. (a) shows the velocity profile emerging due to an immobile interface. No-slip is applicable at the interface. (b) represents a partially mobile interface. The velocity profile is a combination of plug flow and parabolic flow profiles. (c) represents a fully mobile interface that gives rise to plug flow in the film. Image adapted from Janssen and Anderson, 2011

.

dispersed phase within the droplet is very high. As a result, the interface behaves like a solid wall and is immobile. For λ tending to zero, the interface moves freely.

When the continuous phase flows into/out of the film, it experiences resistance to its flow. The flow profile that develops in the film is determined by the nature of this resistance. When the interface is immobile, it behaves like a solid wall. The resistance to the flow in the film is due to the shear stress exerted by a solid wall on the film. As a result, we expect a parabolic velocity profile to develop in the film. For freely mobile interfaces, the interface behaves like a free surface. Resistance to flow is due to resistance to deformation or acceleration of the film itself (Chesters, 1991) and the flow in the film is plug-like. For moderate viscosity ratios, the interface is partially mobile. It is neither a solid wall nor a free-shear layer. The extent to which the interface can move depends on the viscosity of the dispersed phase. The velocity profile is a combination of a plug-like flow profile and a parabolic flow profile (see figure 2.2).

2. Offset ratio

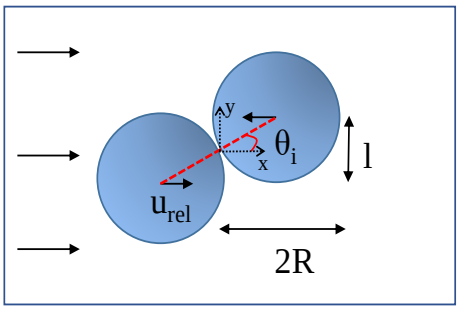

Figure 2.3: Schematic of offset collisions where the line joining the center of the droplets makes an angle with the flow direction of the continuous phase.

An offset collision is a non-head-on collision where the line joining the centers of the droplets makes an angle with the flow direction of the continuous phase. The offset ratio can be defined as the ratio of the shortest distance between the center of the two droplets, l (see figure 2.3), to the diameter of the droplet at the moment of impact. Equivalently, the offset ratio can also be defined by an angle, the impact angle θ_i, such that,

$$\theta_{\mathrm{i}} = \tan^{-1} \frac{l}{2R}$$

An offset/glancing collision differs from a head-on collision in some aspects. After the droplets come in contact with each other, they begin to rotate about a common axis that passes through their point of contact and is normal to plane in which their interfaces touch (an axis parallel to the z-axis and passing through the point of contact of the interfaces in figure 2.3). After rotating to a new configuration such that each of their centers has translated a distance $\sim$ 2R, the droplets begin to separate from each other. Therefore, the time for which the droplets are in contact is finite. The offset ratio determines the actual time available for the droplets to be in contact. For large offset ratios, the actual contact time is decreased. Furthermore, in offset collisions, the force pushing the droplets together is time-dependent (Leal, 2004, Janssen and Anderson, 2011).

3. Capillary number, Ca

The capillary number, Ca, characterizes the deformability of the interface when subjected to shear forces. It is the ratio of the viscous shear force acting to deform the droplet to the surface tension force that resists the deformation. At high Ca, the interface undergoes large deformations.

$$Ca = \frac{\text{viscous forces}}{\text{surface tension force}} = \frac{\mu_c \dot{\gamma} L^2}{\frac{\sigma}{L} L^2} = \frac{\mu_c \dot{\gamma} L}{\sigma}$$

where $\dot{\gamma}$ is the strain rate in the flow field and L is the relevant length scale in the problem. In this problem, L $\sim R$ where R is the radius of the droplets. Therefore, we have

$$Ca = \frac{\mu_c \dot{\gamma}\, R}{\sigma}$$

It is worth noting that the Ca is not only determined by the properties of the continuous phase and the interface but also by the flow conditions. To illustrate this, we can interpret the Ca as the ratio of two velocities, the relative velocity of the droplets, and the characteristic velocity in the film.

$$Ca = \frac{\dot{\gamma} R}{(\sigma/\mu_{\mathrm{c}})}$$

where $\frac{\sigma}{\mu_{\mathrm{c}}}$ is the capillary-viscous velocity scale.

2.1. Parallel-disk model for film drainage

With the given physical description of the problem, we introduce a model, developed by Chesters (Chesters, 1991), for the process of film drainage. Film drainage is the rate-limiting step of coalescence (Kamp et al., 2017) and hence, modeling the film drainage time should explain for the coalescence time - time duration between apparent contact between droplets and coalescence. The model presented in this section is the drainage model for a head-on collision between two identical droplets. While the framework of this model can be used for droplets undergoing offset collisions as well, we need to account for the time-dependent nature of the force pushing the droplets towards each other.

In this model, the processes of approach and film drainage are partially decoupled. As mentioned earlier, the film drainage process is preceded by the approach of the two droplets. Therefore, it is necessary to consider both processes while developing a model for film drainage. A way to partially decouple the two processes is to divide the problem into an 'external problem' corresponding to the

flow of the continuous phase that leads to the approach of the droplets and an 'internal problem' corresponding to the drainage of the thin film between the droplet interfaces (Chesters, 1991). By doing this, we assume that the only way the global flow influences the drainage is by providing the force that pushes the droplet interfaces towards each other.

We, now, present the nomenclature used in this model. Two droplets of equal radii, R, approach each other. The force that pushes them towards each other, F_{hyd}, is provided by the flow of the continuous phase or the 'external problem'. The pressure in the center of the thin film is represented as p_{f}, the pressure of the continuous phase far away is p_{a} and the pressure within the droplet is p_{d}. We assume that p_{a} and p_{d} are always constant. The thickness of the film is represented as $h(t)$ and the radius of the film is a (see figure 2.4).

The hydrodynamic force F_{hyd}, pushing the droplets towards each other is the Stokes drag (Chesters, 1991) on the droplet and can be written as

$$F_{\mathrm{hyd}} \sim \mu_{\mathrm{c}} \dot{\gamma} R^2, \tag{2.1}$$

where $\dot{\gamma}$ is the strain rate in the flow field. F_{hyd} is the viscous shear force exerted by the continuous phase on the droplets.

As the droplets are pushed towards each other by F_{hyd}, the continuous phase is squeezed out of the region between the droplets. Eventually, a thin film of the continuous phase separates the two droplets. Obtaining a model for the drainage rate of this thin film is the objective of this model. F_{hyd} is balanced by a pressure force that originates in the film. By approximating this film as a lubrication layer, we can apply lubrication theory to determine the pressure distribution in the film. The pressure distribution in the film is such that the highest pressure arises in the center of the film, represented as p_{f}, and reduces towards the edge of the film, where the pressure is p_{a} (Reynolds, 1886). The resulting pressure gradient across the film causes the drainage of the film. However, the increase in the pressure within the film also leads to a change in the curvature of the droplet interfaces through the Young-Laplace equation. The resulting deformation of the droplet interfaces determines the radius of the film, a, between the two droplets.

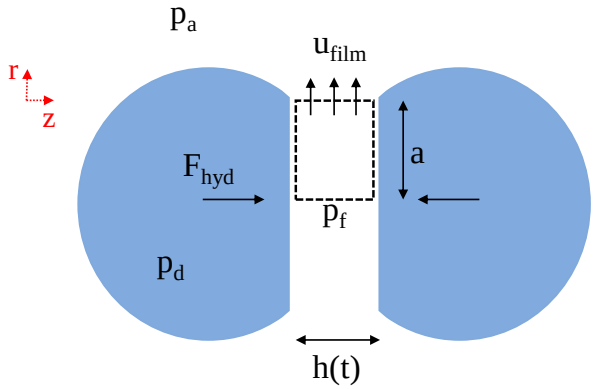

Figure 2.4: A representation of the control volume of the film over which mass and momentum balances are made. The droplet interfaces are assumed to be flat.

The parallel-disk model for film drainage assumes that the deformation of the droplet interface is such that the droplet interface is flat and the film region is disk-shaped as shown in figure 2.4. By assuming that the droplet interfaces are flat, the Young-Laplace equation implies that we limit this model to represent the cases where the maximum pressure in the film, p_{f}, is equal to the pressure of the dispersed

phase within the droplet, p_{d}. Therefore, the difference in pressure of the continuous phase in the center of the film, p_{f}, and just outside the film, p_{a}, is given by

$$\Delta P_{\mathrm{lub}} = p_{\mathrm{f}} - p_{\mathrm{a}} = p_{\mathrm{d}} - p_{\mathrm{a}} \sim 0\left(\frac{2\sigma}{R}\right) \tag{2.2}$$

By setting up a force balance between the hydrodynamic force pushing the droplets towards each other and the resisting lubrication force we arrive at a scaling for the radius of the film, a.

$$F_{\mathrm{hyd}} \sim \Delta P_{\mathrm{lub}} \times \pi a^2$$

$$F_{\mathrm{hyd}} \sim \frac{2\sigma}{R} \times \pi a^2 \tag{2.3}$$

Substituting for F_{hyd} from equation 2.1, we get

$$a \sim \frac{RCa^{1/2}}{\sqrt{2\pi}} \tag{2.4}$$

From equation 2.4, we see that the film radius increases with Ca and R. Mass balance on the film on the control volume marked in figure 2.4 yields,

$$\frac{\partial \int\int\int_{CV} \rho dV}{\partial t} = -\int\int_{CS} \rho u_{\mathrm{film}} dS\ ,$$

where u_{film} represents the velocity of the flow of the continuous phase in the film. By assuming the drainage problem to be axi-symmetric,

$$\pi a^2 \frac{\partial h}{\partial t} = -2\pi a h u_{\mathrm{film}}$$

$$u_{\mathrm{film}} = -\frac{a}{2}\frac{1}{h}\frac{\partial h}{\partial t} \tag{2.5}$$

We obtain another expression for u_{film} by applying a force balance over the thin film. The stresses acting on the control volume are shown in figure 2.5. The force originating from the pressure gradient, ΔP_{lub}, is balanced by the shear stress exerted on the film. Applying a force balance on an element of thin film by assuming the flow in the film to be axis-symmetric, we obtain

$$\tau \times 2\pi a^2 = \Delta P_{\mathrm{lub}} \times 2\pi a h\ , \tag{2.6}$$

where τ represents the shear stress acting on the film. The correct scaling for the shear stress on the film is dependent on the mobility of the interface. For an immobile interface, τ is equivalent to the shear stress exerted by a solid wall on the film. Here, we derive the scaling relation for a partially mobile interface. In the case of a partially mobile interface, the viscosity of the dispersed phase is significant as compared to that of the continuous phase. However, it is not so high as to prevent any movement of the interface. Rather, the dispersed phase exerts a force on the film by virtue of its dynamic viscosity, μ_{d}. For partially mobile interfaces, we scale τ with this force.

The shear stress exerted by the dispersed phase on the film is equal (but opposite in direction) to the shear stress exerted by the film on the dispersed phase. The shear stress exerted by the film on the dispersed phase causes a flow of the dispersed phase within the droplet, referred to as the internal circulation of the droplet (see the velocity profile marked within the droplets by the red lines in

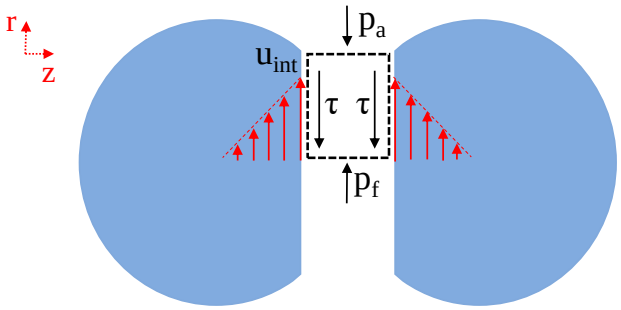

Figure 2.5: A representation of the control volume of the film over which momentum balance is made. The problem is simplified to be axi-symmetric.

figure 2.5). As a result, the shear stress on the dispersed phase exerted by the flow in the film can be estimated as,

$$\tau = \frac{\mu_d u_{\text{int}}}{a}, \tag{2.7}$$

where the length scale over which the flow is estimated to exist within the droplet scales with the radius of the film, a (Chesters, 1991) and u_{int} represents the velocity of the interface.

Substituting for τ from equation 2.7 into equation 2.6, we have

$$\frac{\mu_d u_{\text{int}}}{a} \times a = \frac{2\sigma}{R} \times h$$

From this, we have that

$$u_{\text{int}} = \frac{2\sigma}{\mu_d} \times \frac{h}{R} \tag{2.8}$$

The variation in the velocity of the film is negligible in the regime we consider. Therefore, the velocity of the film, u_{film}, is almost equal to the velocity of the interface, u_{int}. By equating equation 2.8 and 2.5 and substituting for the film radius from equation 2.4, we obtain an expression for the drainage rate as,

$$\frac{1}{R}\frac{\partial h}{\partial t} \sim -\frac{2^{5/2}\pi^{1/2}\dot{\gamma}}{\lambda Ca^{3/2}}\left[\frac{h}{R}\right]^2 \tag{2.9}$$

$$\frac{1}{h^2}\frac{\partial h}{\partial t} \sim -\frac{2^{5/2}\pi^{1/2}\dot{\gamma}}{\lambda Ca^{3/2}}\left[\frac{1}{R}\right] \tag{2.10}$$

From equation 2.9, the negative sign on the right-hand side of the equation suggests that the film thickness reduces with time. This is what we expect from the drainage process. Further, we also see that the rate of change of film thickness is proportional to h^2. This means that as the film thickness decreases, the rate at which the drainage proceeds is also reduced. This suggests that the last stages of drainage are the rate-limiting steps of the process (Chesters, 1991).

By integrating equation 2.10 from the initial film thickness to the critical rupture thickness, we can obtain the expression for the drainage time.

$$\int_{h=h_i}^{h=h_{cr}} \frac{1}{h^2}\partial h \sim -\frac{2^{5/2}\pi^{1/2}\dot{\gamma}}{\lambda Ca^{3/2}}\left[\frac{1}{R}\right]\int_{t=0}^{t=t_{dr}} \partial t$$

$$-\left[\frac{1}{h_{\mathrm{cr}}}-\frac{1}{h_{\mathrm{i}}}\right]\sim-\frac{2^{5/2}\pi^{1/2}\dot{\gamma}}{\lambda Ca^{3/2}}\left[\frac{1}{R}\right]t_{dr} \tag{2.11}$$

Assuming that $h_{\mathrm{i}} \gg h_{\mathrm{cr}}$,

$$t_{\mathrm{dr}}\sim\frac{\lambda Ca^{3/2}}{2^{5/2}\pi^{1/2}\dot{\gamma}}\frac{R}{h_{\mathrm{cr}}} \tag{2.12}$$

The critical rupture thickness, h_{cr}, is expected to depend on the radius of the droplet, R (Leal, 2004).

Oftentimes, we would like to know if two droplets that collide with each other will coalesce or not. For a collision to result in coalescence, the time for film drainage must be shorter than the time for which the droplets are in contact. We can estimate the time scale for droplet contact as,

$$t_{\mathrm{c}}\sim\frac{R}{u_{\mathrm{rel}}}\sim\frac{R}{\dot{\gamma}R}, \tag{2.13}$$

which is the time taken by the droplets to be advected by the flow across a distance, R. We assume that once the droplets have traveled a distance ~ R after they came in contact with each other, they must no longer be in contact (see the expected relative motion of the droplets from figure 2.3).
By comparing the two-time scales, we have

$$\frac{t_{\mathrm{dr}}}{t_{\mathrm{c}}}\sim\frac{\lambda Ca^{3/2}R}{2^{5/2}\pi^{1/2}h_{\mathrm{cr}}} \tag{2.14}$$

For $\frac{t_{\mathrm{dr}}}{t_{\mathrm{c}}}>1$, the collision of two droplets will not lead to coalescence. This is because the time taken for the film to drain is higher than the time for which the droplets are in contact with each other. Therefore, by setting $\frac{t_{\mathrm{dr}}}{t_{\mathrm{c}}}\sim 1$, we can define a condition based on Ca, namely Ca_{cr}, such that for $Ca > Ca_{\mathrm{cr}}$ a collision does not lead to coalescence.

$$Ca_{\mathrm{cr}}\sim\left[\frac{2^{5/2}\pi^{1/2}h_{\mathrm{cr}}}{\lambda R}\right]^{2/3} \tag{2.15}$$

The scaling for t_{c} breaks down for a perfectly head-on collision. This is because, in such cases, contact time is infinite since the droplets are trapped in a stagnation point. From this, it follows that the Ca_{cr} for a head-on collision is infinity.

We, now, summarize our findings from the parallel-disk model. This is done to easily compare the predictions of the parallel-disk model with the results from experimental studies that will be discussed in the next section.

1. The drainage time, t_{dr}, for perfectly-head on collisions scales as $Ca^{3/2}$ (see equation 2.12).
2. The drainage time,t_{dr}, for perfectly-head on collisions increases with λ (see equation 2.12).
3. The Ca_{cr} for offset collisions decreases with the offset ratio because contact time between droplets is decreased at high offset ratios.
4. The Ca_{cr} for offset collisions decreases with the radius of the droplet, R, and scales with the viscosity ratio as $Ca_{\mathrm{cr}}\sim\lambda^{-0.68}$ (see equation 2.15).

Few remarks need to be made regarding the assumptions of this model. This model assumes that the shape of the droplet interface remains flat and drainage occurs out of a disk-shaped film whose thickness is invariant in space and decreases in time. However, this is an approximation. It has been

proven that a flat film cannot be sustained. This is because drainage occurs faster at the edge of the flat film over the small length where the curvature of the interface changes. As a result, the film becomes dimple-shaped (Yiantsios and Davis, 1990). Secondly, all the discussion made in this chapter including this model is based on the underlying assumption that coalescence is triggered when two droplets approach each other. While this seems like a reasonable assumption to make, we will see in the following section that some experimental observations reported in the literature qualify this assumption. Therefore, it is important to recognize this assumption we have made in our discussion of coalescence so far.

2.2. Experimental studies

Experiments that focus on the systematic study of collision events between two droplets are reviewed here. After briefly mentioning the various experimental set-ups used in coalescence studies, we present an elaborate discussion on the results of experimental studies. As mentioned previously, the parallel-disk model for film drainage is developed based on the assumption that coalescence is initiated when two droplets approach each other. The discussion in this section will indicate that while coalescence can be driven by approach, it is not the only means to trigger coalescence. Experimental results indicate that the coalescence of two droplets can also be triggered by the separation of the two droplets. This being said, from this point on, a distinction is always made between the two mechanisms for coalescence as 'approach-driven coalescence' and 'separation-driven coalescence'. Therefore, the discussion in this section is categorized into two parts - approach-driven coalescence and separation-driven coalescence. While discussing approach-driven coalescence, the results from experiments will also be compared with the predictions of the parallel-disk drainage model. In our discussion of separation-driven coalescence, we present theories and experimental results related to this phenomenon.

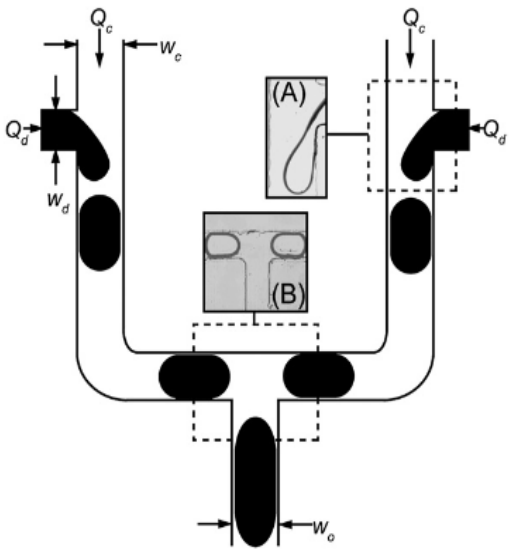

Figure 2.6: The T-junction used by Christopher et. al to realise collisions Christopher et al., 2009. The image illustrates the need for generating droplets synchronously and bringing them to the central T-junction to realise collisions. This can be a serious limitation to such junction-based microfluidic devices used for coalescence studies.

Macroscopic experimental set-ups to study the collision and coalescence of pairs of identical dropletss in a viscous flow make use of shearing flow fields that can be generated using sliding glass plates (Guido and Simeone, 1998), the four-roll mill (Leal, 2004), and Couette devices (Mousa et al., 2001). Figure

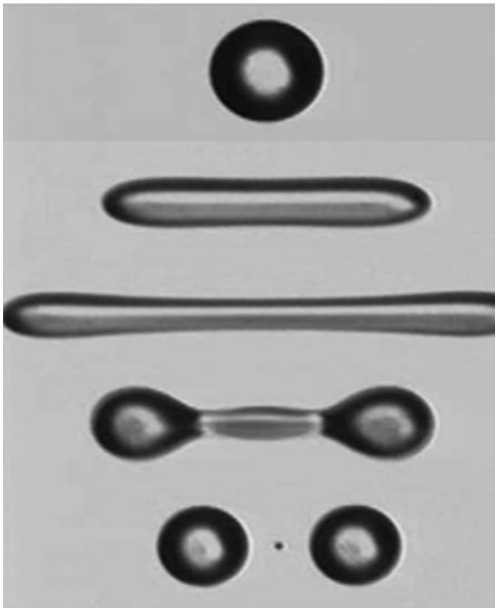

Figure 2.7: The pictures represent the protocol used to generate droplets. High shearing rates are used to stretch the droplet. When capillary instabilities are significant, the external flow is shut off and the droplet breaks up naturally. Note the formation of a small satellite droplet in between the two daughter droplets.Image adapted from Leal, 2004

2.7 shows the protocol adopted to generate droplets by using the external shear field. Droplet generation and collisions are controlled by manipulating the external flow (Leal, 2004, Guido and Simeone, 1998, Mousa et al., 2001). Microfludic platforms have also been exploited to study the coalescence of droplets. Devices incorporate passive strategies such as sudden expansions in the channel (Bremond et al., 2008), junctions in the channel as shown in figure 2.6 (Christopher et al., 2009, Wang et al., 2013) and surface patterning (Fidalgo et al., 2007) to enable collisions between droplets.

The results from these studies are discussed in the subsequent paragraphs. We first discuss approach-driven coalescence and evaluate the parallel-disk film drainage model in light of the experimental results. Following this, we discuss separation-driven coalescence.

2.2.1. Approach-driven coalescence

The mechanism for approach-driven coalescence has been discussed in detail in this chapter. When two droplets approach each other, a thin film of the continuous phase is formed between them. When this thin film drains up to a critical thickness, the film ruptures and coalescence is initiated. The parallel-disk model for film drainage is developed based on this understanding of approach-driven coalescence and the predictions of the model were summarized in section 2.1. The experimental results related to approach-driven coalescence is discussed here.

We summarize the results from the seminal study on droplet coalescence by Leal, 2004 in the four-roll mill. Experimental results show that the drainage time for perfectly head-on collisions, t_{dr}, scales as $Ca^{3/2}$ and $\lambda^{-0.8}$. In the case of offset collisions, Ca_{cr} was experimentally found to decrease with the radius of the droplet as $Ca_{\mathrm{cr}} \sim R^{-5/6}$. From this, it is concluded that, $h_{\mathrm{cr}} \sim R^{-1/4}$ (from equation 2.15). Further, for low viscosity systems ($\lambda < 0.1$), the Ca_{cr} is found to decrease with the offset ratio. This is a natural consequence of the decrease in available contact time between the droplets with an increase in offset ratio. On comparing these experimental findings to the predictions of the drainage model, we see that the scaling model captures the physics of the process for over a limited range of Ca and λ.

Having addressed the range of experimental data that support our current understanding of approach-driven coalescence, the instances where the model fails are presented. Firstly, at very low Ca ($< 10^{-3}$), experimental data suggest that the drainage time for a head-on collisions become invariant with the Ca (Baldessari and Leal, 2006). This is not what we expect from the scaling model derived in section 2.1 that suggests that the t_{dr} decreases monotonically with the Ca (see equation 2.12). Secondly, experimental data from offset collisions between droplets aren't satisfactorily explained by the parallel-disk model. For high viscosity ratio systems, $\lambda > 0.1$, it was seen that the Ca_{cr} does not decrease monotonically with an increase in offset ratio. Rather, at higher offset ratios, Ca_{cr} starts to increase (Leal, 2004). This observation is counter-intuitive to our current understanding of approach-driven coalescence.

Furthermore, in complete disagreement with the mechanism of approach-driven coalescence, droplets were observed to coalesce when the force acting on the droplets tries to pull them apart (Leal, 2004, Guido and Simeone, 1998, Bremond et al., 2008). This phenomenon is described as separation-driven coalescence, where coalescence is not preceded by the approaching of two droplets, rather, coalescence seems to be triggered when the droplets begin to separate from each other. From these observations, it appears that there exists another regime where droplets coalesce, namely, separation-driven coalescence, that cannot be reconciled with the understanding of coalescence that was presented so far and requires a discussion of its own.

2.2.2. Separation-driven coalescence

Initial reports of separation-driven coalescence are from 2004 (Leal, 2004) and since then, several attempts have been made to investigate this phenomenon and characterize this regime of coalescence. In an experimental study of coalescence in microfluidic channels, droplets were made to encounter a sudden expansion in the channel following which they entered a constriction in the channel (see figure 2.8). It was observed that the droplets did not coalesce when pushed against each other (in the expansion) but coalescence occurred when the leading droplet entered the constriction in the channel (see figure 2.8a). By investigating the distance between the centers of the two droplets, it was concluded that the droplets coalesced when they started to separate from each other (Bremond et al., 2008).

This interesting discovery begs the question- what is the mechanism for separation-driven coalescence? A hypothesis was proposed based on the pressure distribution inside a lubrication film between two separating interfaces. While the pressure in the thin film increases when interfaces approach each other, separating interfaces gives rise to a suction pressure in the thin film (Reynolds, 1886), which is necessary to drive the flow of the continuous phase into the film region. However, the interface between a droplet and the continuous phase is not rigid, the suction pressure within the film causes the droplet interfaces to deform towards each other leading to a local thinning of the thin film, thereby driving coalescence (Leal, 2004). In support of this hypothesis, the formation of nipples has been captured (as shown in figure 2.8b) in the contact area between separating droplets (Bremond et al., 2008).

Using this hypothesis, a model for separation of droplets to drive coalescence was derived (Lai et al., 2009) based on the argument that the time scale related to the deformation of the interfaces, t_{def}, must be smaller than the time scale at which the center of mass of the droplets are pulled apart by the external flow, t_{sep}. The model was applied to the experimental set-up of Bremond et al., 2008 and their experimental results were used to validate the model developed in this study. It was found analytically that the time taken for the deformation to grow sufficiently to trigger coalescence varied inversely with how quickly the droplets were separated from each other. This was also observed from the experimental

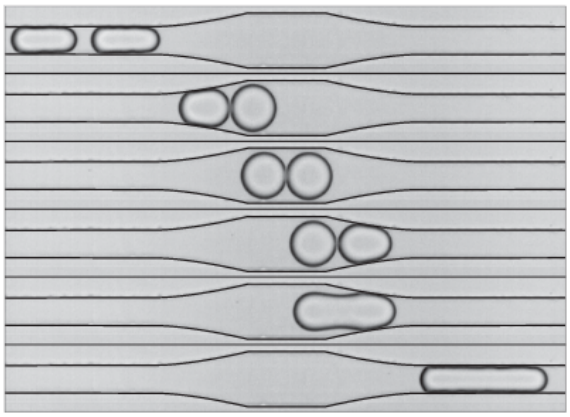

(a) The microfluidic expansion used by Bremond et. al in their study. The pancake shaped droplets assume a spherical shape on entering the expansion. Coalescence is observed when the centre-to centre distance of the droplets begin to increase.Image adapted from Bremond et al., 2008

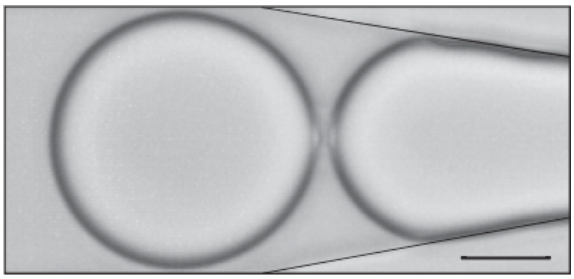

(b) The formation of nipples on the droplet interfaces suggesting the presence of low pressure in the film as the droplets begin to separate. Image adapted from Bremond et al., 2008

Figure 2.8: The study of Bremond et al., 2008 in microfluidic channels with a sudden expansion-constriction section in the channel.

data of Bremond et al., 2008. The agreement between the model and the experimental results adds evidence to the hypothesis.

Furthermore, studies have found an experimental condition that is defined based on the Capillary number, Ca, such that for $Ca > Ca_{cr}$, separation between droplets does not lead to coalescence (Gunes et al., 2013,Chatzigiannakis et al., 2020). The existence of a Ca_{cr} for separation-driven coalescence is yet to be clearly understood. Note that we do not expect the Ca_{cr} of separation-driven coalescence to be the same as the Ca_{cr} of approach-driven coalescence. The focus of this study is separation-driven coalescence and any further reference to a Ca_{cr} corresponds to the critical Ca of separation-driven coalescence. To the best knowledge of the author, there exists no work that has determined the dependency of the Ca_{cr} on the system parameters, namely, λ and the offset ratio.

In summary, two regimes in which droplets coalesce seem to exist- an approach-driven coalescence and separation-driven coalescence. The parallel-disk model for film drainage assumes that the approach of two droplets must trigger coalescence. From experimental results, the model seems to represent head-on collisions reasonably but falls short in its predictions over the outcome of offset collisions. Separation-driven coalescence is a relatively new discovery from experimental studies and we are yet to entirely understand the mechanism for this regime of coalescence. A hypothesis proposed in the literature attempts to explain the mechanism behind separation-driven coalescence. Also, experimental studies report the existence of a condition based on the Ca, such that for $Ca > Ca_{\mathrm{cr}}$, separation ceases to trigger coalescence. To further validate the hypothesis, we need to investigate if the hypothesis can explain the presence of a Ca_{cr}.

2.3. Research objectives

The study of Leal, 2004 using the four-roll mill is the most extensive study on shear-induced coalescence in which macroscopic parameters such as the drainage time has been measured. This highlights the need to design other systematic experimental set-ups to study this phenomenon to corroborate or refute the currently available experimental data. The reproducibility and repeatability of the collision and coalescence events with macroscopic experimental setups are questionable (Guido and Simeone,

1998). Microfluidic devices for coalescence studies, where high control over droplets can be achieved, have undesirable characteristics such as non-repeatable collisions, need for synchronous droplet generation (see figure 2.6), and multi-droplet fusion.

In this thesis, we aim to

1. Develop a microfluidic device in which both approach-driven coalescence and separation-driven coalescence can be systematically studied.
2. Experimentally investigate the presence of the critical capillary number for separation driven coalescence Ca_{cr} and determine the dependency of Ca_{cr} on the viscosity ratio λ and offset ratio.
3. Develop a scaling model to explain the presence of Ca_{cr}.

The study will be restricted to droplets and the behaviour of bubbles will not be the focus of this thesis. Furthermore, while most systems of practical relevance use surfactants (Leal, 2004), as a first step, we perform studies without surfactants to reduce the complexity of the process. Finally, it is re-iterated that any reference to Ca_{cr} in the following chapters refers to the critical Ca corresponding to separation-driven coalescence unless explicitly stated otherwise.

3

Design of the flow device and Experimental set-up

In this chapter, the design approach of the experimental set-up is discussed. Rapid-prototyping is adopted as the workflow methodology. It allows us to progress based on action and observation rather than assuming a theoretical approach towards finding the optimized design. The design of the flow device, the fabrication method, and the experimental set-up are discussed. Finally, the dimensions of the finalized prototype are presented and justified.

3.1. Design approach

Microfluidic devices used in coalescence studies use geometric configurations or surface patterning to enable collision between two droplets. In general, it is challenging to control the angle of collision between two droplets in these devices. While the confinement provided by the walls of the microfluidic channel improves the repeatability in the motion of a train of droplets, the motion of individual droplets cannot be controlled. Microfluidic devices in which droplets are forced to collide at junctions in the channels (refer figure 2.6) have the added disadvantage of necessitating synchrony in the motion of droplets to ensure the collision of droplets at the junction.

We propose a microfluidic device in which droplet collisions are repeatable and controllable. Monodisperse droplets will be produced in a T-junction and carried through the channels by the flow of the continuous phase. The motion of each droplet will be guided by designing features in the channel based on the concept of surface energy wells, thereby, making the collisions more controllable. In this section, we explain and motivate the major choices that contribute to the proposed design of the microfluidic chip.

3.1.1. Microfluidics

Microfluidics offers an ideal framework to study coalescence because of the small scales that characterize the flow. Due to these small scales, high strain rates can be achieved in microfluidic devices (Stone et al., 2004). Confined droplets can be controlled owing to their high sensitivity towards the presence of channel walls. This eliminates the need for active controls to manipulate the droplet po-

sition and movement. Furthermore, advancements in fabrication methods that are cost-effective and fast (Duffy et al., 1998, McDonald et al., 2000) make it possible to employ a rapid prototyping work-flow methodology.

Droplet generation

Droplet generation in microfluidic devices can be very precise and reliable. Several configurations of microfluidic channels- T-junctions, Y-junctions and cross-flow junctions- have been used to create droplets in microfluidic devices (Glawdel et al., 2012, Link et al., 2004). The continuous phase enters the device through a 'main' channel and the dispersed phase enters the device through an 'inlet' channel (see figure 3.1). The main channel and inlet channel meet at a junction where the dispersed phase is split by the continuous phase and droplets are generated. Droplets are generated from an interplay of viscous forces, pressure forces, and capillary forces. Depending on the dominant forces, various regimes are identified in the droplet generation process within micro-fluidic channels and the regimes are briefly discussed in this section.

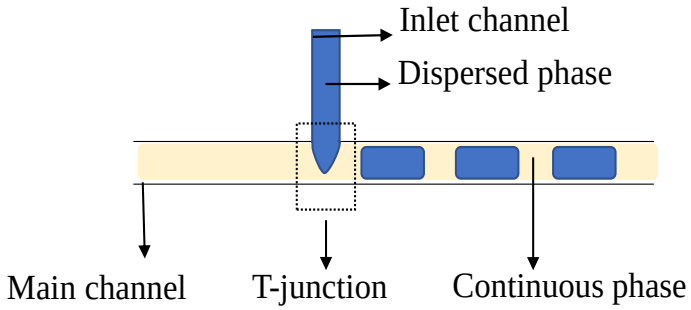

Figure 3.1: An illustration of the droplet generation process in a microfluidic T-junction device.

Three regimes have been identified based on the dominant forces that govern the droplet break-up - the squeezing regime (particular to microfluidic channels), the dripping regime, and the jetting regime. In microfluidic devices, the effects of the channel walls cannot be neglected. The squeezing regime is a consequence of the dispersed phase blocking a large part of the main channel when flowing out of the inlet channel. As a result, the continuous phase is forced to flow through a small gap between the interface of the droplet and the channel wall. The pressure upstream of the interface increases and squeezes the neck, initiating a breakup. In this regime, the size of the droplet is independent of λ and Ca, but depends only on the ratio of the flow rates (Xu et al., 2005). In the dripping regime, shear forces exerted by the continuous phase on the dispersed phase cause an elongation of the neck and drives break-up. Studies conclude that the dripping regime in confined microfluidic channels is significantly modified from unconfined droplet generation. This is attributed to the fact that the dispersed phase always blocks a significant part of the main channel. As a result, the effects of the pressure build-up of the continuous phase cannot be entirely neglected (De Menech et al., 2008). They also report that the dripping regime exists over a small range of Ca and is hard to realize in experimental conditions. As a result, no scaling relation could be proposed for the effect of the parameters on the droplet size.

Surface Energy Wells

Surface energy wells take advantage of the tendency of any fluid system to minimize its interfacial area and uses this principle to trap droplets. When we introduce a spherical droplet, of radius R, into

a microfluidic channel whose depth, h, is smaller than the diameter of the spherical droplet, then the droplet is forced to deform and assume a pancake shape that is energetically less favorable to the droplet, as shown in figure 3.2. Such a 'confined' droplet is extremely sensitive to variations in the height of the channel (Dangla et al., 2011). By carving small wells or traps into the channel floor (or bottom/top walls), we can force a confined droplet to remain attached to the well where a part of the droplet interface within the well assumes a spherical cap shape as illustrated in figure 3.3 by the blue region. The force that enables the droplet to remain in the well is the gradient in the surface energy of the droplet and this force opposes the drag force from the continuous phase. When the hydrodynamic drag force on the droplet exceeds the force originating from the local reduction in surface energy, the droplet is pulled out of the well (Dangla et al., 2011). These traps are called surface energy wells and can be used to both capture droplets and to guide them (Abbyad et al., 2011).

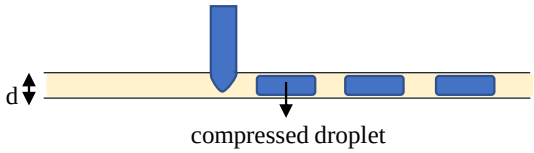

Figure 3.2: Front cross-sectional view of a droplet generated at a microfluidic T-junction where the height of the channels are smaller than the unconfined radius of the droplet. The droplet is compressed and assumes a pan-cake shape.

To develop a microfluidic platform for droplet coalescence studies, we propose to trap, position, and guide the collision of droplets using surface energy wells (refer figure 3.4). Anchors can trap a droplet up to a critical flow rate of the background phase. The critical flow rate depends on the geometry of the anchor and the size of the droplets (Abbyad et al., 2011). Below the critical flow rate, the anchor always traps a droplet. However, when a free-moving droplet comes within the interaction range of the trapped droplet, two different modes were observed by Abbyad et al., 2011. The free-moving droplet can replace the trapped droplet in the anchor (buffer mode) or the free-moving droplet can slide past the trapped droplet (parking mode) after making contact. Additionally, by using sinusoidal patterning over their channel walls, they demonstrated that rails can be used to guide the droplet through predefined trajectories. Based on the results of their study, we have attempted to use surface energy wells for trapping and guiding droplets to realize repeatable collisions for droplet coalescence studies.

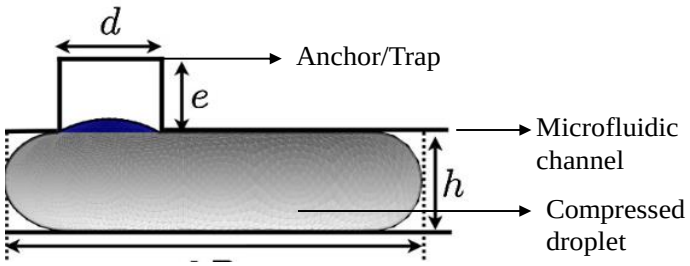

Figure 3.3: The image shows the cross-sectional side view of a confined droplet trapped in an anchor. The confined droplet can locally re-assume a spherical shape (blue shaded region in the image) and decrease its surface energy. In this image, h is the depth of the channel, d is the diameter of the anchor and e is the depth of the anchor. Image adapted from Dangla et al., 2011

Figure 3.4 represents an illustration of the proposed microfluidic device. The anchor is a small well (similar to the well shown in figure 3.3) where we intend to trap a droplet. The rail is also a surface energy well, however, unlike an anchor it extends along a direction. Rails are grooves that are etched on the channel surface and can be used to guide the droplets. In the proposed design, the droplets are first produced at the T-junction shown in figure 3.4. The generated droplets will be carried by the

continuous phase to the anchor. One droplet is trapped at the anchor. By operating at the parking mode, we can ensure that any subsequent droplet only interacts with the trapped droplet, but does not replace it in the anchor. The purpose of the rail is to guide the motion of subsequent droplets such that we have control over the point of collision. Therefore, the rail is designed such that it extends from the T-junction towards the anchor. Hence, the droplets follow the pathway dictated by the rail, like how a train is guided by tracks, and collide with the trapped droplet at the intended point.

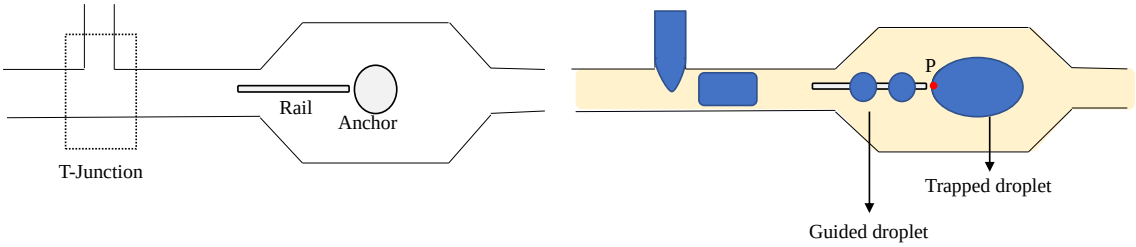

Figure 3.4: An illustration of the proposed design of the device.

In figure 3.5, a particular advantage of adding rails to the design is illustrated. By having rails, we are not limited to collisions along the center-line of the channel (depicted by the dashed line in figure 3.5) but by positioning the rail appropriately in the design, we can obtain collisions between the trapped droplet and guided droplet at any position. To illustrate this, the point P (depicted as the red dot) in figure 3.4 and figure 3.5 shows the expected point of collision in the two designs that differ from each other in the position of the rail.

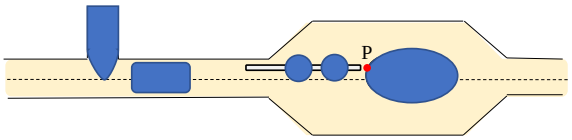

Figure 3.5: A device in which the rail is offset from the centre line of the channel (dashed lines) by a distance. By changing the position of the rail, we can vary the point of collision between the trapped droplet and the guided droplet.

Having discussed the main features of the device, we explain the method used to fabricate the device.

3.2. Fabrication method

In this section, we describe the fabrication process adopted for making the microfluidic devices. Microfluidic chips are made by casting a polymer over a master mold. The master mold is designed on AUTODESK and uploaded to the Form 3 3-D printer from Formlabs. The 3-D printer is an ideal choice for rapid prototyping since the mold can be printed within a few hours. After printing, the molds are flushed with an air gun to remove the liquid resin attached to the mold. Since the features in the design are comparable to the resolution of the printer, removing any liquid resin that remains in the mold is necessary to obtain sharp features. The mold is then washed with isopropyl alcohol for 20 minutes. At the end of this cleaning step, the molds are once again flushed using an air gun. After this, the mold is washed for a second time for 10-15 minutes. The mold is then cured in a UV station for 2-3 hours at 60 °C.

The UV cured mold is surface treated with Trichloro (1H,1H,2H, 2H-perfluorooctyl) silane overnight. This is done by placing the mold within a vacuum bell along with a Petri dish with 2-3 drops of Trichloro (1H,1H,2H, 2H-perfluorooctyl) silane. The vacuum bell is closed and vapors of Trichloro (1H,1H,2H,

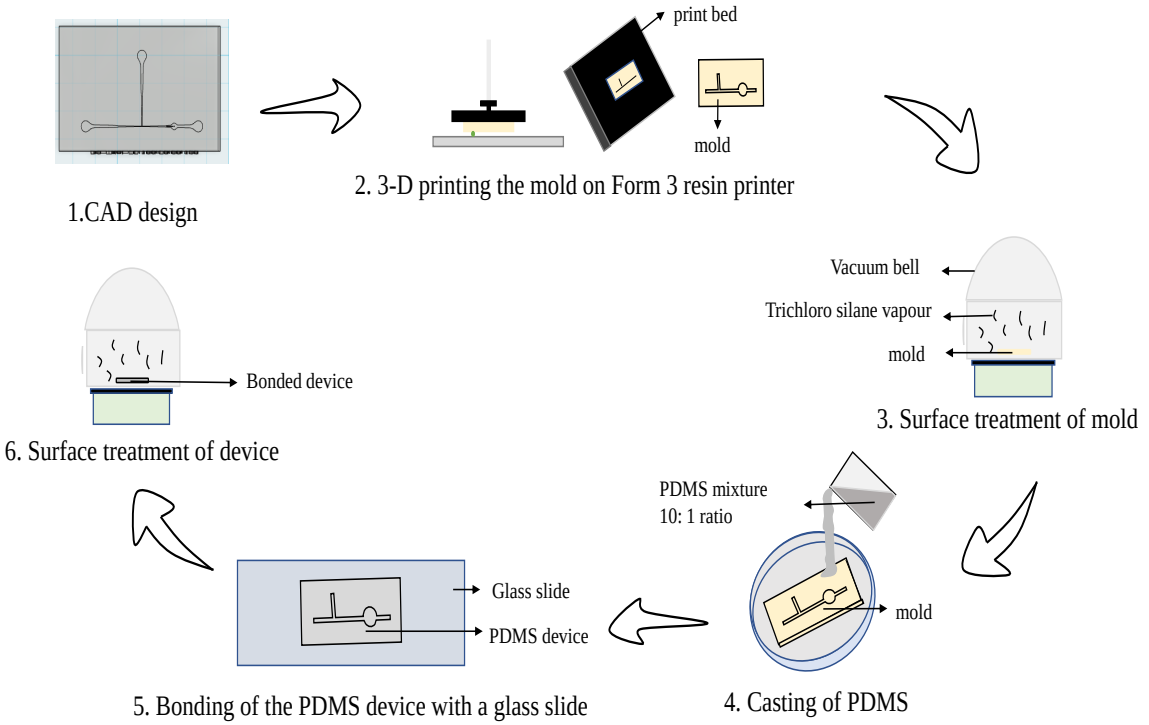

Figure 3.6: An illustration showing the fabrication process adopted in this thesis

2H-perfluorooctyl) silane are created by maintaining a low pressure of 100 mbar within the chamber, as shown in step 3 of figure 3.6. Surface treating the mold helps in the 'peeling off' of the cast polymer in the subsequent steps.

After surface treating the mold, a degassed mixture of elastomer base and curing agent (Polydimethylsiloxane or PDMS) is poured over the mold. The PDMS is prepared by mixing the base and curing agent in the ratio of 10:1. We choose to make the flow device out of PDMS due to its optical transparency, softness, and elasticity (Whitesides, 2006). The softness of PDMS allows us to punch holes into the device so that tubes can be plugged in. The elasticity of PDMS forms a natural seal around the tubes and prevents leakage. The mold-mixture system is kept inside the oven at 65 °C for 10-12 hours. After letting the cured PDMS cool down, we peel the PDMS device off the mold.

The device is, then, bonded to a glass slide. The bonding is carried out by spin-coating a thin layer of PDMS on the glass slide and partially curing the thin layer of PDMS by placing the glass slide in the oven at 65 °C for 25-30 minutes. The partially cured PDMS serves as the bonding agent for the device and the glass slide and also forms the bottom wall of the channel. The bonded device is, then, cured at 65 °C for 8-10 hours.

Finally, the fabricated device is once again subject to surface treatment with Trichloro (1H,1H,2H, 2H-perfluorooctyl) silane. Surface treatment is performed over the bonded device to make the channel walls hydrophobic. Wall effects have a big influence on microfluidic operations. Firstly, the phase which is present inside the droplet is determined by which phase prefers to wet the wall (Joanicot and Ajdari, 2005). Making the walls hydrophobic ensures that only the continuous phase (oil) wets the wall and water droplets are formed. Furthermore, the roughness of the 3-D printed molds can cause water droplets to stick to the walls of the channel leading to the failure of the experiment. The hydrophobic nature of the walls also ensures that the water droplets are repelled by the wall surface.

3.3. Experimental setup

Figure 3.7 illustrates the experimental setup used to test the prototypes. The microfluidic chip is placed on an inverted Nikon Ti microscope that is connected to a high-speed camera. The field-of-view of the microscope focuses on the interrogation area that is represented in figure 3.7. Videos are captured at 3000 fps. We use such a high frame rate since typical coalescence times are of the order of $10^{-3}s$. Two syringe pumps are used to push oil and water into the flow device. Oil and water are generally chosen as the working fluids in microfluidic devices as higher viscosity liquids will suffer large pressure drops while flowing through a microfluidic channel. (Janssen and Anderson, 2011).

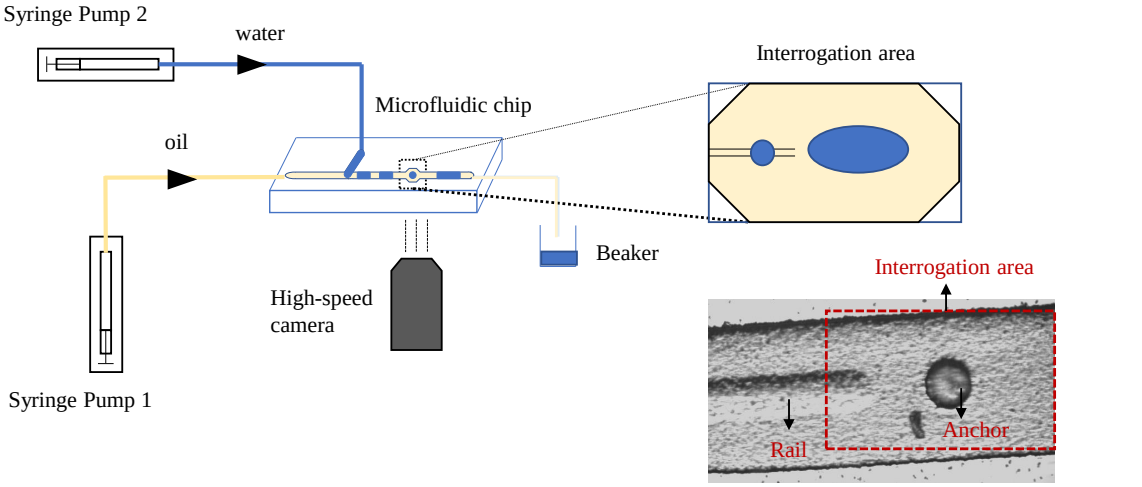

Image of the interrogation area from the real device. Droplets are not present in the shown image.

Figure 3.7: An illustration showing the experimental set-up for testing the prototypes

The protocol followed while filling the device is discussed here (Christopher et al., 2009). The tubing is connected to two identical syringes filled with oil and water, respectively. Syringes are carefully filled with working fluids to avoid the introduction of air bubbles. The fluid is manually pushed out of the syringe so that the fluids enter the tubing and fill the entire length of the tube. This is done to prevent the syringe pump from forcing air into the microfluidic channel. The syringes are then placed in the syringe pump. The tubing for the oil phase is attached to the oil inlet. The outlet is connected to a beaker for collecting the oil-water mixture. The tubing to the water inlet is not attached to the device, yet. The channels are filled with the oil phase first so that the oil wets the channel walls. The water phase is allowed to enter the device through the inlet channel later. First, syringe pump 1 (see figure 3.7) is switched on and the oil phase fills all the channels. After the oil phase has filled the channel, syringe pump 1 is switched off and syringe pump 2 (for water) is switched on. The tubing for the water phase is attached to the water inlet hole. When the water phase enters the channel and reaches the T-junction, syringe pump 1 is also switched on. The pressures in the channels are allowed to settle down before any data is recorded.

3.4. Design constraints

Based on the phenomena we want to study (namely, coalescence), the chosen fabrication method, and the chosen measurement technique, there are some constraints on the design of the device. The constraints and their implications on the design are discussed below.

The droplet size should be minimized: Smaller droplets are more resistant to deformation than larger droplets. As a result, they maintain their shape and this translates to a smaller error while approximating the shape of the droplets. The size of the droplet is determined by the width of the T-junction since the droplet fills the channel in a microfluidic device (De Menech et al., 2008). Hence, we minimize the size of the T-junction.

The dimensions of the channels should be higher than the resolution of the 3-D printer: The resolution of the 3-D printer is 25 μm in the z plane. The smallest feature attainable in the xy- plane is nearly 80 μm in size, which corresponds to the width of the laser dot. This determines the lower limit that we can reach by using the 3-D printer to fabricate our mold. When approaching the resolution of the printer, errors become comparable to the dimensions of the feature itself. Hence, we restrict ourselves to a lower limit of 200 μm in the xy plane and 50-75 μm in the z plane.

The device should fit within a microscopic glass slide (~ 25 mm ×75 mm): Since we use optical microscopy to observe the phenomenon, the device has to be bonded with a glass slide through which we view the oil-water system. As a result, the dimensions of the device are constrained by the glass slide that can be placed in the holder of the microscope.

Design should minimize the pressure drop within the channel (preferable): The pressure drop in a microfluidic device can be very high (Stone et al., 2004) due to viscous fluids flowing through channels of small dimensions. As a result, it is preferred that the smallest dimensions (width of the T-junction) aren't maintained throughout the device.

3.5. Device dimensioning

In this section, the design of the device used for this study is justified. Figure 3.8 shows the dimensions of the device that are to be identified. Based on the constraints posed in section 3.4, the dimension to be minimized is the width of the T-junction, w_{t}, which determines the size of the droplet formed. The minimum dimension that can be realized in this device is dictated by the XY resolution of the 3-D printer. From our experience, we find that the lower limit to the features in the XY plane is around 200 μm. Apart from w_{t}, the width of the rail, w_{r}, is also to be minimized. This is necessary to allow for maximum control over the point of collision between the free-moving droplet and the trapped droplet. Hence, w_{r} is also around 200 μm. Based on this estimation for the width of the rail, the diameter of the anchor, d_{a}, is set to 300 μm. The width of the channel at the interrogation area, w_{i}, is designed to be four times the sum of the radius of the trapped droplet (~ radius of the anchor) and the radius of the free-moving droplet (~ 0.5 ×width of the T-junction), which is 1000 μm. This design choice is made to reduce the influence of the wall on the behavior of the colliding droplets.

The depth of the channel, h_{c}, is determined based on the expected radius of the droplet and the z resolution of the 3-D printer. Since we aim to use surface energy wells to our advantage, we need to generate compressed droplets in the device (see figure 3.2). Therefore, the height of the channel must be less than the expected radius of the droplet, which is about 100 μ m. It is, thus, chosen that the height of the channel, h_{c} is around 70-80 μm, which is also three times the Z resolution of the 3-D printer. The depth of the anchor, h_{a}, plays an important role in the trapping strength of the anchor. From experimentation, we find that the trapping strength of the anchor increases as the depth of the anchor is increased, within the range of anchor depths tested (50 μm to 175 μm). Based on the range of Ca we intend to study in the experiments (~ 10^{-2}), h_{a} is determined to be around 150-180 μm. The height of the rail, h_{r}, is minimized since the functionality of the rail is merely to guide the droplets. Increasing

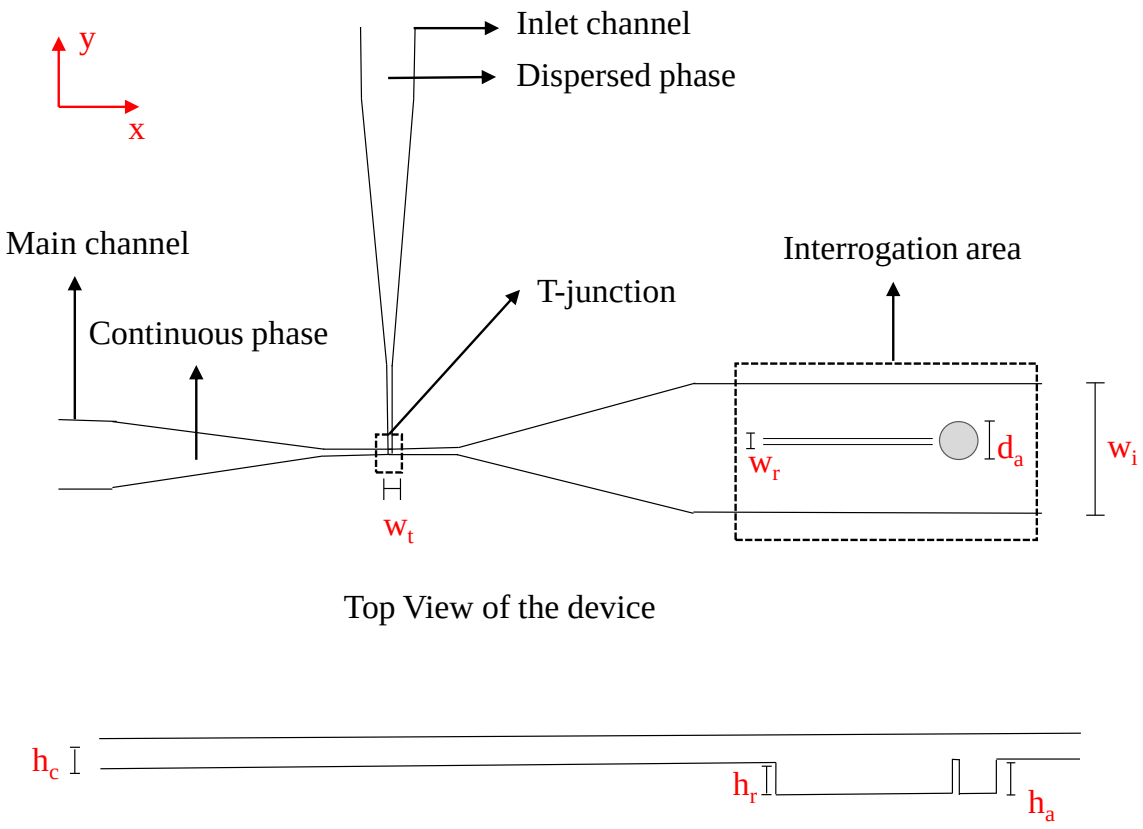

Figure 3.8: Schematic showing the dimensions of the device to be designed.

the depth of the rail makes it harder to push the droplets out of the rail near the anchor. Hence, h_r set between 25-50 μm.

In figure 3.9, the images of the microfluidic device are presented. Figures 3.9a and 3.9b correspond to the top view of the T-junction and interrogation area respectively, which is also marked in figure 3.8. It is evident from these images that the surface of the channels is very rough. This is a consequence of fabricating the devices from a 3-D printed mold. In figure 3.9c and figure 3.9d, a cross-sectional view of the channel is shown. To obtain the images, we first create cross-sections of the device by carefully cutting across the device, through a cross-sectional plane, with a sharp knife. The chosen cross-sectional plane is the y-z plane in figure 3.8. The sections are, then, placed on a clean glass slide and observed under the microscope. Figure 3.9c is the cross-sectional view of the main channel near the T-junction. We see from the image that the cross-section is not rectangular as one would expect, but rather is rounded near the edges. Figure 3.9d is a cross-section of the channel, farther away from the T-junction, where the rail is placed. The increase in depth of the channel at the middle of the image (see the red box in figure 3.9d) indicates the position of the rail. We notice, once again, that the channel edges are not sharp but rather rounded. This is also an effect of the fabrication method. The 3-D printer does not have a high enough resolution to make molds of sharp edges for the dimensions that we require. Therefore, there is always a discrepancy between the designed dimensions and the measured dimensions in the device.

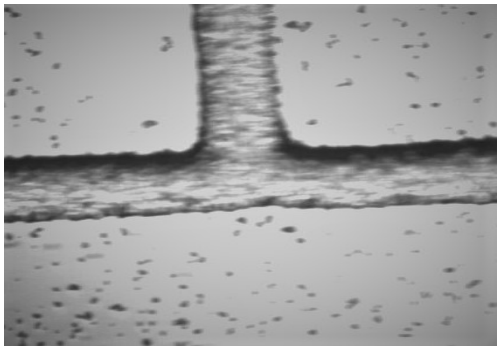

(a) A picture of the T-junction of the device.

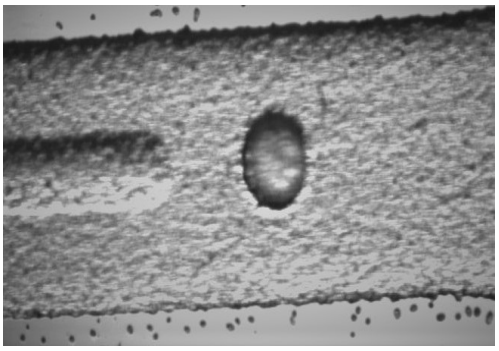

(b) A picture of the interrogation area of the device showing the end of the rail and the anchor.

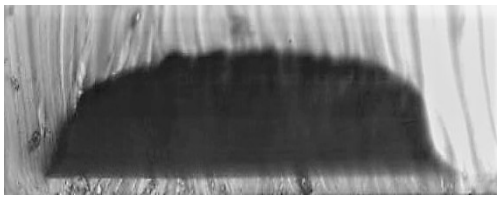

(c) A cross-sectional view of the channel. Cross-section is taken close to the T-junction and channel width is close to 300 μ m.

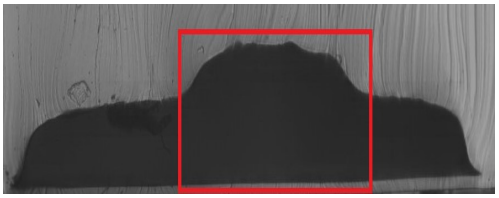

(d) A cross-sectional view of the channel area in which the rail is positioned at the middle of the channel as per the design. The red box on the image indicates the rail. It can be seen that the rail is not exactly in the center of the channel, but is skewed towards the right. This could be a result of an error in the fabrication of the mould.

Figure 3.9: Pictures of the microfluidic device while viewed through the microscope. The roughness of the channel surface is evident in the pictures.

4

Results and Discussions

In this section, the findings from this work are presented and interpreted. Firstly, the design proposed in section 3.5 is tested for repeatability and control over droplet collisions. Secondly, the findings concerning the effect of the governing system parameters, namely the offset ratio (or equivalently, the impact angle θ_i) and the viscosity ratio (λ), over the critical Capillary number (Ca_{cr}) of separation-driven coalescence is discussed. A simple scaling model predicting this dependency of Ca_{cr} is derived and it is compared against experimental data.

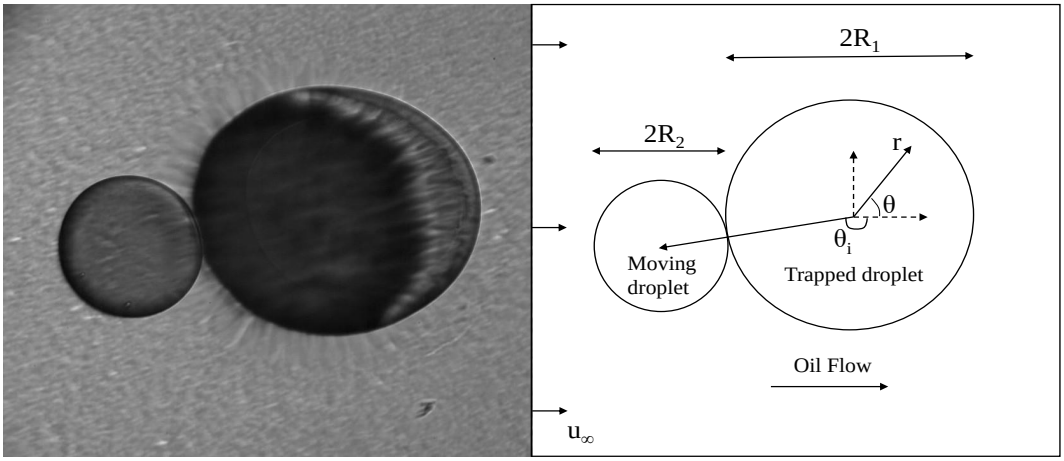

Figure 4.1: *(Left)* Image shows the interrogation area at the moment of impact between two droplets. *(Right)* Schematic representing the interrogation area.

Before proceeding to the results, the geometry of the problem and the nomenclature used in the following chapters is introduced. The interrogation area consisting of the trapped droplet and the moving droplet is shown in figure 4.1. The flow of oil is from the left to right. In all experiments, the continuous phase is mineral oil (light, Sigma-Aldrich). Experiments are performed by using two different fluids as the dispersed phase, namely DI water and a glycerol-DI water mixture. The in-plane curvature of the trapped droplet is approximated to be equivalent to a circle of radius R_1 and equal to the radius of the anchor. The radius of the free-moving droplet is referred to as R_2. The velocity of the continuous phase, oil, far away from the anchor is referred to as u_∞.

The cylindrical coordinate system (r,θ) is chosen with the axis placed at the center of the trapped droplet to describe the flow field. Since the flow is symmetrical about the x-axis, we compute θ such that $\theta \in [0\ \pi]$. The impact angle, θ_i, is defined as the angle made by the line joining the center of the two droplets with the positive x-axis at the moment of impact.

4.1. Repeatability and control over collisions

The objective behind the proposed microfluidic device is to enable repeatable and controllable collisions. Apart from applications in droplet-based microfluidics, it is a crucial step towards building an experimental set-up for the systematic study of shear-induced droplet coalescence. In this section, the proposed design is marked based on these characteristics - namely repeatability and control of droplet collisions, over hundreds of recorded collision events.

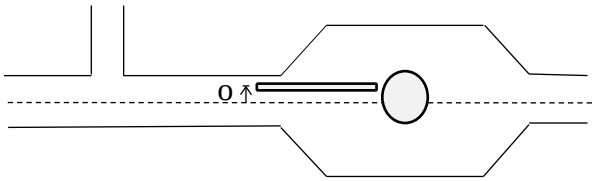

Figure 4.2: An image showing the positioning of the rail in the device.

The success of the design is evaluated by comparing the performance of the proposed design of the device (see section 3.5), hereafter referred to as the experimental device, against a control device. The control device is defined as a device that does not have rails and is similar to the experimental device in other aspects. Droplet coalescence experiments are performed with both devices and data of over hundreds of collisions are recorded and compared. An experimental data set is defined as the data obtained from an experimental device such that the rails are positioned to facilitate a specific impact angle of collision between the droplets. In figure 4.2, O marks the distance of the center of the rail from the centerline of the channel. By varying the value of O in the design, the rails are positioned to facilitate different impact angles. In this regard, three different experimental devices, device 1, device 2, and device 3, corresponding to distinct positions of the rail are tested. Since all experiments performed with the control device are of the same design, all the data from these experiments fall into one single data set corresponding to the control device. It is important to mention that the control device used for this comparison is similar in design but not of the same dimensions as the experimental device, as would be generally assumed. Experiments performed on a control device of the same dimensions as the experimental device were largely unsuccessful, in the sense that a large number of observable events did not involve a collision between the two droplets (see figure 4.3). This is because, as shown in figure 4.3, the droplets tend to drift towards the sidewalls of the channel and fail to collide with the trapped droplet in the interrogation area.

The frequency distribution of the impact angle is plotted in figure 4.4 to visualize the performance of the experimental device against the control device. A narrow and distinct peak is identified in each data set corresponding to an experimental device (figure 4.4a). Similarly, a single peak can be observed in the data from the control device corresponding to a high impact angle 4.4b). From a first glance, it is already clear that the selectivity of impact angles is higher in the case of the experimental device, where three distinct peaks can be spotted across the range of impact angles, θ_i, between 90°and 180°. To quantify the repeatability of collisions, we define the variable p as the fraction of occurrence of the most occurred impact angle interval against the total number of collisions considered. Control over droplet

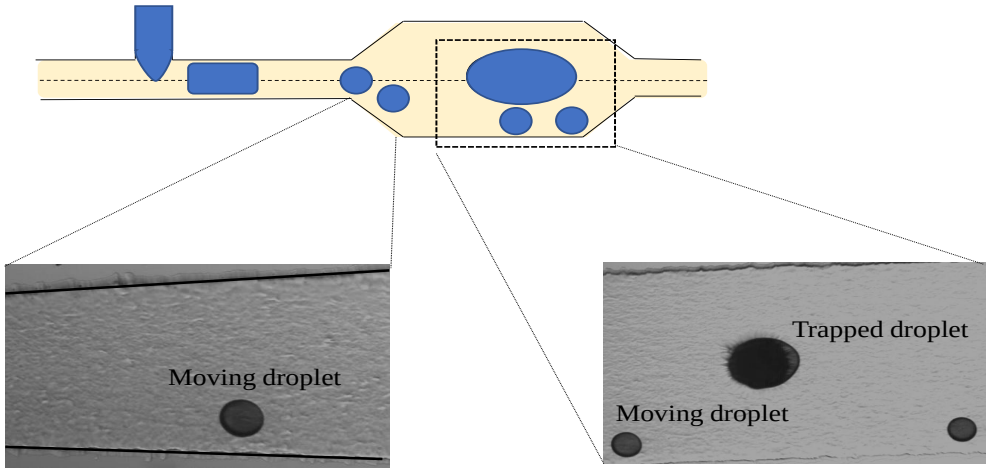

Figure 4.3: An image showing the drifting of droplets from experiments on a control device of the same dimensions as the experimental device.

collisions is characterized by the spread of the impact angle in each experimental data set which is computed as the range of the data set, r, and the selectivity over the impact angle is represented by the number of peaks in the distribution.

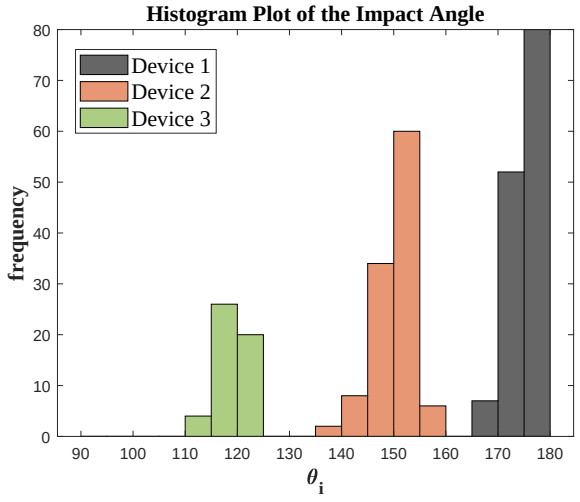

(a) The frequency distribution of impact angles obtained from three experimental devices. Three distinct peaks are observed corresponding to the three devices.

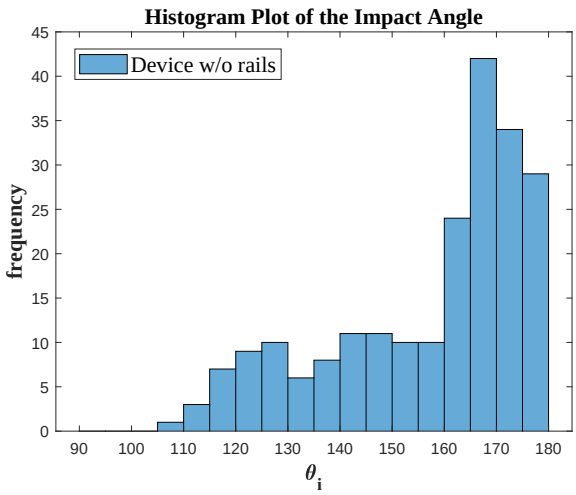

(b) The frequency distribution of the impact angles obtained on the control device.

Figure 4.4: Histograms representing the distribution of impact angles.

From the results presented in table 4.1, it is clear that the experimental device outperforms the control device in enabling repeatability of collisions. The value of the parameter p is over 50% for all the experimental devices while it is only 12 % for the control device. This is because the most frequently occurring impact angle is determined by the positioning of the rail in the case of the experimental device. In the case of the control device, the frequently occurring impact angle is between 170-165°. In principle, the droplets are generated at the T-junction and carried by the background phase, here the oil phase. They are expected to behave as particles that follow the flow. After the droplets are generated at the middle of the channel, they are expected to follow the centerline of the channel and

Device		p	r	no of peaks in the distribution
Experimental Device	Device 1	0.575	13.31	3
	Device 2	0.545	21.25	
	Device 3	0.52	12.41	
Control Device		0.12	70.16	1

Table 4.1: Table listing the performance parameters of the experimental and control devices

collide with the trapped droplet at a high impact angle. However, most droplets tend to drift from the expected trajectory. One possible reason could be due to hydrodynamic interactions between droplets that can lead to instabilities (Beatus et al., 2012). Asymmetry in the geometry of the channel could also lead to particle drift. The p value in the control device is, thus, an estimate of the stability of the droplets along their natural trajectory. By comparing the p values, it is evident that the preferred impact angle is more often encountered in the experimental device owing to the preference over specific impact angles that is enabled by the rails.

The spread of the impact angle, r, is also significantly larger for the control device indicating that it is not possible to have a narrow distribution of impact angles. While a peak can be identified at low impact angles, the data spread over a range of 70°. On the contrary, the range of impact angles encountered in each experimental device is 10-20°, suggesting a narrow distribution around the preferred impact angle. Lastly, it is not possible to control the position of the peak encountered in the control device. In other words, the preferred impact angle of collision will always be restricted to high impact angles. This is represented by another parameter, namely the number of peaks, which can be increased in the experimental device through the position of the rail. In the design, the rail can be positioned to suit our choice of impact angle. However, in the fabrication of the device, the center of the rail can only be changed in steps and the value of this step depends on the resolution of the fabrication method. As a consequence of this, the impact angles can also be changed only in steps. With the current fabrication method, it was difficult to sample the angles between 175°, 150°, and 120°.

From our experiments, we conclude that the use of surface energy wells can enhance the control over droplet collisions in microfluidic devices. Furthermore, we find that the designed device can be used as part of an experimental setup to study droplet coalescence.

4.2. Study of droplet coalescence

In this section, an introduction to the flow field in the interrogation area is given. An overview of the experimental observations is also provided. Following this, we proceed to summarize our results from the coalescence studies.

4.2.1. Characterizing the flow field

To develop a model, it is important to characterize the flow in the device. In this subsection, we introduce a framework through which we can theoretically describe the flow field in the interrogation area. The flow geometry in the interrogation area corresponds to a Hele-Shaw flow cell with an aspect ratio ($\frac{w_i}{h_c}$) = 13.33. By applying the Hele-Shaw approximations, we can consider the depth-averaged flow field to be rotation-free (Hele-Shaw, 1898). As a result, the flow field around the trapped droplet is modeled as the ideal flow around a cylinder of radius R_1. Following this, we have that

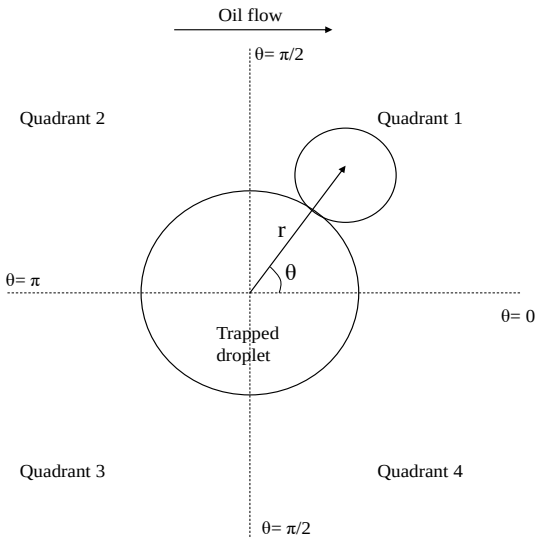

Figure 4.5: A schematic of the interrogation area divided into four quadrants.

$$u_r(r,\theta) = u_\infty \left(1 - \left(\frac{R_1}{r}\right)^2\right)\cos(\theta)\,, \tag{4.1}$$

$$u_\theta(r,\theta) = -u_\infty \left(1 + \left(\frac{R_1}{r}\right)^2\right)\sin(\theta)\,, \tag{4.2}$$

$$e_{rr}(r,\theta) = \frac{2u_\infty R_1^2 \cos(\theta)}{r^3}\,, \tag{4.3}$$

where u_r is the radial velocity, u_θ is the tangential velocity and e_rr is the radial strain in the flow field. For the period in which the two droplets are in contact, the radial coordinate of the center of the free moving droplet can be approximated as r= $R_1 + R_2$. Therefore, as an estimate of the forces and velocity of the free moving droplet, equations 4.1, 4.2 and 4.3 are computed at r= $R_1 + R_2$. By doing this, we approximate the free moving droplet to be a point particle in the flow field that follows the flow. This is, however, an approximation.

As can be seen from figure 4.5, the flow field is divided into 4 quadrants. From equation 4.1, we see that the radial velocity is positive in quadrant 1 and quadrant 4 because the sign of the cosine function is positive. This means that when the moving droplet is in either of these two quadrants, the moving droplet is separating away from the trapped droplet. In quadrant 2 and quadrant 3, the sign of the cosine function is negative, and hence the moving droplet is pushed towards the trapped droplet in these quadrants. Note that e_rr also follows the sign of u_r.

The only non-dimensional number that depends on the flow field is Ca. Ca is defined as

$$Ca = \frac{\mu_c U}{\sigma}, \tag{4.4}$$

where U represents a velocity scale, μ_c represents the viscosity of the oil phase and σ represents the interfacial tension. We choose U $\sim E_\mathrm{rr} L$ such that it characterizes the maximum relative velocity between the two droplets as their centers are at a distance of $R_1 + R_2$. Note that, the trapped droplet is stationary and the relative velocity between the droplets is directly the velocity of the free moving droplet. Here, E_rr represents the maximum radial strain rate and L is the length scale of the 'external

problem' that is governed by the flow of the continuous phase and is defined in the subsequent section. From this, we can define the Ca corresponding to the problem as,

$$Ca = \frac{\mu_c E_{rr} L}{\sigma} \tag{4.5}$$

The Ca is defined such that it represents the non-dimensional relative velocity between the two droplets that can be entirely determined based on experimental conditions as it only depends on fluid properties, the geometry of the droplets, and u_∞.

$$Ca = \frac{E_{\mathrm{rr}} L}{\frac{\sigma}{\mu_c}} = \frac{\text{maximum relative velocity scale}}{\text{capillary} - \text{viscous velocity scale}} \tag{4.6}$$

$\frac{\sigma}{\mu_c}$ represents the capillary-viscous velocity scale - the only velocity scale that results from the two dominant forces governing the problem - capillary forces and viscous forces. In this work, the Ca is interpreted as a ratio of velocity scales rather than a ratio of forces. Equivalently, Ca can be interpreted as the competition between two velocity scales - the velocity scale related to the separation of centers of the two droplets and a velocity scale related to the lubrication problem in the film between the two droplets. By this means, we can connect the 'external problem' that is governed by the flow of continuous phase to the 'internal problem' that is governed by the flow in the film region between the droplet interfaces.

With the stated framework for characterizing the flow field, we proceed to discuss some of the observations from the experiments that guide this research work.

4.2.2. Experimental observations

We present an elaborate description of the experiment. First, the design of the experiment is presented. We, then, present some observations from the experiment. The work in this thesis is guided by these observations, hence, it is important to discuss them to appreciate the course of this research.

Experiments are performed by varying three parameters, the impact angle θ_i, the viscosity ratio λ, and the Capillary number, Ca. Three different impact angles are chosen, namely 175°, 150°, and 120°. Experiments were performed with two systems- a DI water- mineral oil system with λ= 0.033 and a glycerol-DI water mixture- mineral oil system with λ= 0.2. Values for the interfacial tension of σ = 20.5 mN-m for the DI water-mineral oil interface and σ = 12.5 mN-m for the glycerol-DI water mixture-mineral oil interface, as reported in literature, was used (Posocco et al., 2016, Sinzato et al., 2017).

Six sets of experiments were performed, each consisting of a particular combination of λ and θ_{i}. For each experimental set, the flow rate of oil is increased in small steps and videos of the collision events are recorded at each step. By changing the flow rate of the oil phase, we can change the Ca defining the experimental condition. The measured parameters were the impact angle θ_{i} and time duration, t, between impact and coalescence of the two droplets. The videos were recorded at 3000 fps.

We noticed in our experiments that while the impact between droplets occurred in quadrant 2 or quadrant 3 (refer to figure 4.5), we never observe coalescence in these two quadrants where droplets are pushed towards each other, according to equation 4.1. Rather, if the droplets coalesced, it always occurred in quadrant 1 and quadrant 4. An example of this is shown in figure 4.6. As discussed previously, the droplets separate away from each other in quadrant 1 and quadrant 4. We, thus, conclude that the coalescence between the two droplets observed in our experiments is separation-driven.

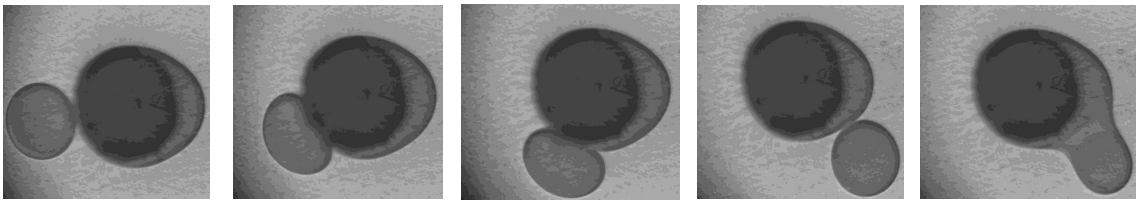

Figure 4.6: A time series representing a collision event that led to coalescence, Ca= 0.0018, $\lambda = 0.033$, $\theta_i = 175°$

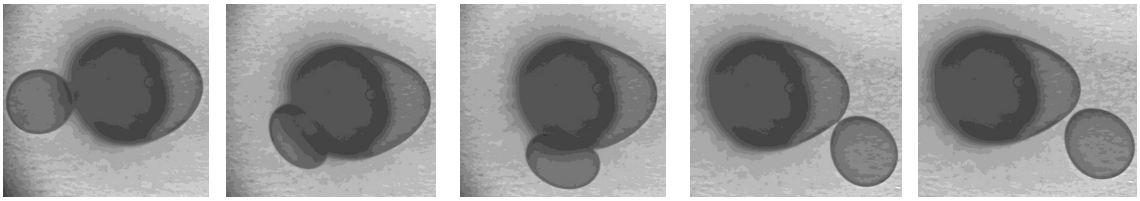

Figure 4.7: A time series representing a collision event when the droplets separated without coalescing, Ca= 0.0029, $\lambda = 0.033$, $\theta_i = 175°$

We make another interesting observation from our experiments. Figure 4.6 shows a collision event that was recorded for an experimental set of λ= 0.033 and θ_i = 175 °at $Ca = 0.0018$. When we increase the flow rate of the oil phase, we increase the Ca. On increasing the Ca, we started observing collision events that did not lead to coalescence even upon separation. Such an event, at a $Ca = 0.0029$, is shown in figure 4.7. Furthermore, we also observed that the number of collision events that did not result in coalescence increases with Ca. From this observation, we suspect that by gradually increasing the Ca, for each set, we will reach an experimental condition when the number of collision events resulting in coalescence decreases to zero. We refer to the Ca defining this experimental condition, where the separation between droplets ceases to drive coalescence, as the Ca_{cr}.

Based on these observations, we conclude that under the experimental conditions maintained, coalescence is driven by the separation of droplets. Further, we also expect that there exists an experimental condition defined by Ca_{cr} at which separation between droplets ceases to trigger coalescence. We, now, proceed to investigating the Ca_{cr}. We explain the presence of Ca_{cr} through a scaling model and proceed to compare the predictions of this model with our experimental results.

4.2.3. Simple scaling model to predict Ca_{cr}

In our experiments, we observe coalescence when the moving droplet was about to separate away from the trapped droplet. We conclude that the coalescence of the two droplets is triggered by their separation. Further, we also observe an experimental condition based on the non-dimensional relative velocity (Ca) between the droplets such that for, $Ca > Ca_{cr}$, separation of droplets ceases to trigger coalescence.

In this subsection, we attempt to derive a model to explain the presence of a Ca_{cr} for separation-driven coalescence. Firstly, we briefly state the hypothesis attempting to explain separation-driven coalescence. The model to predict the Ca_{cr} is developed based on this hypothesis. The approach adopted in this model for predicting the Ca_{cr} is also presented. Following this, an attempt is made to describe the collision and coalescence process in the current experimental setup. We, then, present the ideas borrowed from the literature that aid in the derivation of the model. Finally, the model is

derived.

It has been proposed that the mechanism for coalescence during separation is local thinning of the film due to the deformation of droplet interfaces in response to the suction pressure that arises in the film between separating interfaces (Leal, 2004). Following this, the model estimates the Ca_{cr} for separation driven coalescence by comparing the two velocity scales that govern the problem - the velocity scale of separation of the droplets, u_{rel}, and the velocity scale governing the deformation of the droplet interfaces in response to the sudden drop in film pressure, $\dot{\tilde{h}}$. We argue that the Ca_{cr} can be found when the velocity scales are of the same order. If $u_{\mathrm{rel}} > \dot{\tilde{h}}$, we do not expect coalescence.

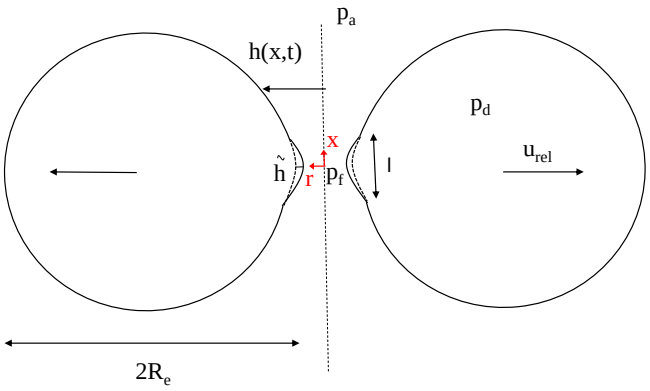

Figure 4.8: Schematic of two separating droplets and the resulting deformation of the interface

Figure 4.1 represents an image of the moment at which the moving droplet impacts the trapped droplet. At this moment, the center of the moving droplet is located at r=$R_1 + R_2$, $\theta = \theta_{\mathrm{i}}$. From the moment of impact, the radial distance of the center of the moving droplet is always described by r=$R_1 + R_2$, until the moment of coalescence or separation. The impact between the two droplets occurs at quadrant 2 or quadrant 3 (refer figure 4.5). After impact, the moving droplet describes a trajectory as shown in figure 4.6 and figure 4.7. If the droplets coalesce, it always occurs in quadrant 1 or quadrant 4. We view this whole process as being composed of two distinct mechanisms favoring coalescence. Invoking the nature of the flow field in the current experimental set-up (see figure 4.1), we see that the problem is one of film drainage as the free moving droplet moves from its impact angle θ_{i} to $\theta = \frac{\pi}{2}$, i.e when the center of the moving droplet falls in quadrant 2 or 3. When the moving droplet enters quadrant 1 from quadrant 2 or quadrant 4 from quadrant 3, the external flow begins to separate the two droplets away from each other. This can be seen from equation 4.1, where the sign of the radial velocity, u_{r}, is positive indicating that the droplet moves along the positive r direction in quadrant 1 and quadrant 4. While coalescence is observed only in quadrant 1 or quadrant 4, we suspect that the film drainage phase influences the outcome of the separation. This is because the film drainage process influences the thickness of the film on the onset of separation. Therefore, this part of the process is also in our interest.

Figure 4.8 represents a schematic of two separating droplets. Although the two droplets in our problem are non-identical (see figure 4.1), we consider the problem to be similar to that of coalescence between two identical droplets of radius , R_{e}, such that (Chesters, 1991),

$$R_{\mathrm{e}} = \frac{R_1 R_2}{R_1 + R_2} \tag{4.7}$$

We assume that the two droplets separate at a velocity $u_{\mathrm{rel}} \sim E_{\mathrm{rr}} R_{\mathrm{e}}$. Therefore, in our definition of Ca

(see equation 4.6), the length scale $L \sim R_e$. It is important to note here that the angle of coalescence(θ_c) is assumed to be $\theta_c = 0$ when $Ca = Ca_{cr}$. We adopt a local coordinate system (x,r) such that x=0 represents the center of the film and h(x,t) represents the interface of the droplets. h_o represents the minimum distance between the two droplets, h(x=0,t), and $\tilde{h}$ represents the maximum deformation of the interface, expected at the center of the film at the moment of separation. Note that h(x=0,t=0) represents the minimum film thickness at the onset of separation and we expect it to be influenced by the film thickness at the end of the drainage process. The pressure in the centre of the film is represented as p_f, the pressure far away is p_a and the pressure inside the droplet is represented as p_d.

Before we begin developing the model, we recognize that some length scales have entered the problem that we currently do not have an estimate for, namely, the film thickness at the end of the film drainage process and the length scale for the deformation of the droplet interface on separation, $\tilde{h}$. Before we derive the model, we first estimate these length scales.

Estimation of film thickness at the end of the film drainage process, h_{min}

We expect the thickness of the film at the end of the film drainage process to influence the outcome of the separation of the two droplets. Therefore, we begin by estimating the film thickness at the end of the film drainage process. To do this, we invoke the parallel-disk model that was presented in section 2.1. We integrate the equation for rate of change of film thickness (obtained for head-on collisions) presented in the aforementioned section, namely equation 2.10, from $\theta = \theta_i$ to $\theta = \frac{\pi}{2}$. Importantly, by doing this, we simplify the film drainage process as drainage of the film through a head-on collision that was allowed to proceed up to a finite period.

$$\int_{h=h_i}^{h=h_{min}} \frac{1}{h^2} dh \sim -\frac{2^{5/2}\pi^{1/2}\dot{\gamma}}{\lambda Ca^{3/2}} \left[\frac{1}{R_e}\right] \int_{t=t(\theta=\theta_i))}^{t=t(\theta=\frac{\pi}{2})} dt \tag{4.8}$$

where h_i represents the initial thickness of the film at the moment of impact and h_{min} is the thickness at the end of the film drainage process, i.e, at $\theta = \frac{\pi}{2}$. It is noted here that $\dot{\gamma}$ is the strain rate based on experimental conditions which is E_{rr} in our problem.

The independent variable t can be found as a function of the angle θ through the relation

$$(R_1 + R_2)d\theta = u_\theta|_{R_1+R_2} dt \tag{4.9}$$

From equation 4.2, we have

$$u_\theta|_{R_1+R_2} = -u_\infty \left(1 + \left(\frac{R_1}{R_1 + R_2}\right)^2\right) \sin(\theta) \tag{4.10}$$

Substituting equation 4.10 into equation 4.9, we have

$$(R_1 + R_2)d\theta = -u_\infty \left(1 + \left(\frac{R_1}{R_1 + R_2}\right)^2\right) \sin(\theta) dt$$

$$dt = -\left[\frac{(R_1 + R_2)}{u_\infty \left(1 + \left(\frac{R_1}{R_1+R_2}\right)^2\right)}\right] \csc(\theta) d\theta \tag{4.11}$$

Substituting equation 4.11 into equation 4.8,

$$\int_{h=h_{\mathrm{i}}}^{h=h_{\min}} \frac{1}{h^2} dh \sim \frac{2^{5/2}\pi^{1/2}E_{\mathrm{rr}}}{\lambda Ca^{3/2}} \left[\frac{1}{R_{\mathrm{e}}}\right] \left[\frac{(R_1+R_2)}{u_\infty \left(1+\left(\frac{R_1}{R_1+R_2}\right)^2\right)}\right] \int_{\theta=\theta_i}^{\theta=\frac{\pi}{2}} \csc(\theta) d\theta$$

Substituting for R_{e}, we have

$$\int_{h=h_{\mathrm{i}}}^{h=h_{\min}} \frac{1}{h^2} dh \sim \frac{2^{5/2}\pi^{1/2}E_{\mathrm{rr}}}{\lambda Ca^{3/2}} \left[\frac{R_1+R_2}{R_1R_2}\right] \left[\frac{(R_1+R_2)}{u_\infty \left(1+\left(\frac{R_1}{R_1+R_2}\right)^2\right)}\right] \int_{\theta=\theta_i}^{\theta=\frac{\pi}{2}} \csc(\theta) d\theta$$

On integrating and substituting the limits, we recognize that that $h_{\min} << h_{\mathrm{i}}$. We therefore have,

$$-\frac{1}{h_{\min}} \sim -\frac{2^{5/2}\pi^{1/2}E_{\mathrm{rr}}}{\lambda Ca^{3/2}} \left[\frac{R_1+R_2}{R_1R_2}\right] \left[\frac{(R_1+R_2)}{u_\infty \left(1+\left(\frac{R_1}{R_1+R_2}\right)^2\right)}\right] \left[\log_e |\csc(\theta_i)-\cot(\theta_i)|\right]$$

$$h_{\min} \sim \frac{\lambda Ca^{3/2}u_\infty}{2^{5/2}\pi^{1/2}E_{rr}} \times \frac{(R_1R_2)\left[1+\left(\frac{R_1}{R_1+R_2}\right)^2\right]}{(R_1+R_2)^2} \times \frac{1}{\log_e |\csc(\theta_i)-\cot(\theta_i)|}$$

For compactness, we represent $\frac{(R_1R_2)\left[1+\left(\frac{R_1}{R_1+R_2}\right)^2\right]}{(R_1+R_2)^2} = g(R_1,R_2)$ which is a known function.

$$h_{\min} \sim \frac{\lambda Ca^{3/2}u_\infty}{2^{5/2}\pi^{1/2}E_{\mathrm{rr}}} \times g(R_1,R_2) \times \frac{1}{\log_e |\csc(\theta_i)-\cot(\theta_i)|}$$

Substituting for E_{rr} we have,

$$h_{\min} \sim \frac{\lambda Ca^{3/2}(R_1+R_2)^3}{2^{7/2}\pi^{1/2}R_1^2} \times g(R_1,R_2) \times \frac{1}{\log_e |\csc(\theta_i)-\cot(\theta_i)|} \tag{4.12}$$

Now, we have an estimate for the thickness of the film at the onset of separation. Now, we direct our attention to the second length scale that we are yet to estimate - the length scale related to the deformation of the interface, $\tilde{h}$.

Estimating the deformation of the interface, $\tilde{h}$

We borrow the idea of Lai et al., 2009 to estimate an expression for the deformation of the interface in response to the suction pressure in the film. We note that the assumptions stated in the derivation of $\tilde{h}$ are the assumptions made in the cited literature (Lai et al., 2009) and are presented here for clarity.

We approximate the problem to be two-dimensional, neglecting the flow in the third dimension corresponding to the height of the channel. Within the Hele-Shaw flow cell, the droplets are pancake-shaped. We assume that any changes in the curvature of the droplet occur only in this 2-D plane and the curvature of the droplet dictated by the height of the channel is unaffected. The droplet interface is assumed to be circular in the instant preceding separation.We assume that the pressure inside the droplet, p_{d}, and the pressure far away, p_{a}, remain constant.

Now, we obtain an estimate of $\tilde{h}$. To do this, we make use of the Laplace boundary condition that relates the curvature of the interface, κ, to the pressure jump across the interface, $\Delta p_{d->f}$.

$$\Delta p_{d->f} = p_{\mathrm{f}} - p_{\mathrm{d}} = \sigma\kappa \tag{4.13}$$

The curvature of a plane curve can be expressed as

$$\kappa = \frac{\frac{\partial^2 h}{\partial x^2}}{\left(1 + (\frac{\partial h}{\partial x})^2\right)^{3/2}} \sim \frac{\partial^2 h}{\partial x^2}, \tag{4.14}$$

where we assume that $\frac{\partial h}{\partial x} << 1$.
Substituting for κ from equation 4.14 into equation 4.13, we have

$$\Delta p_{d->f} = p_{\mathrm{f}} - p_{\mathrm{d}} = \sigma\kappa \sim \sigma\frac{\partial^2 h}{\partial x^2} \tag{4.15}$$

The deformation of the interface in response to the suction pressure developed in the film is treated as a perturbation over the un-deformed curvature of the interface. As a result, the curvature of the deformed droplet is obtained as a linear superposition of the curvature of the un-deformed droplet, $-\frac{1}{R_{\mathrm{e}}}$, and the perturbation that scales as $\frac{\tilde{h}}{l^2}$, where l represents the length scale over which the perturbation exists (see figure 4.8).

$$\Delta p_{d->f} = p_{\mathrm{f}} - p_{\mathrm{d}} = \sigma\kappa \sim \sigma\frac{\partial^2 h}{\partial x^2} \sim \sigma\left(-\frac{1}{R_{\mathrm{e}}} + \frac{\tilde{h}}{l^2}\right) \tag{4.16}$$

We expect $l \sim (R_{\mathrm{e}} h_{\mathrm{o}})^{0.5}$. This formulation for l is the only way to obtain a length scale such that $h_{\mathrm{o}} << l$ and $l << R_{\mathrm{e}}$.

From lubrication theory, we know that the suction pressure in the center of the film p_{f} is related to the pressure far away p_{a} ($p = p_{\mathrm{a}}$ when $x >> l$) by

$$\Delta p_{\mathrm{lub}} = p_{\mathrm{f}} - p_{\mathrm{a}} \sim -\left(\frac{f(\lambda)\mu_{\mathrm{c}} u_{\mathrm{rel}}}{h_{\mathrm{o}}^2}\right) R_{\mathrm{e}} ,$$

$$\Delta p_{\mathrm{lub}} = p_{\mathrm{f}} - p_{\mathrm{a}} \sim -\frac{f(\lambda)\mu_{\mathrm{c}}(E_{\mathrm{rr}} R_{\mathrm{e}}) R_{\mathrm{e}}}{h_{\mathrm{o}}^2} , \tag{4.17}$$

where $f(\lambda)$ is a currently unknown function of the viscosity ratio, λ.
Substituting for p_{f} from equation 4.17 into equation 4.16, we have

$$\Delta p_{d->f} = p_{\mathrm{a}} - p_{\mathrm{d}} - \frac{f(\lambda)\mu_{\mathrm{c}}(E_{\mathrm{rr}} R_{\mathrm{e}}) R_{\mathrm{e}}}{h_{\mathrm{o}}^2} \sim \sigma\left(-\frac{1}{R_{\mathrm{e}}} + \frac{\tilde{h}}{l^2}\right) \tag{4.18}$$

We know that for an un-deformed droplet, the pressure inside the droplet p_{d} is related to the pressure far away p_{a} through the Laplace boundary condition as,

$$\Delta p_{d->a} = p_{\mathrm{a}} - p_{\mathrm{d}} \sim \sigma\frac{\partial^2 h}{\partial x^2} \sim -\sigma\left(\frac{1}{R_{\mathrm{e}}}\right) \tag{4.19}$$

By substituting for $p_{\mathrm{d}} - p_{\mathrm{a}}$ from equation 4.19 into equation 4.18,

$$-\frac{f(\lambda)\mu_{\mathrm{c}}(E_{\mathrm{rr}} R_{\mathrm{e}}) R_{\mathrm{e}}}{h_{\mathrm{o}}^2} \sim \sigma\left(\frac{\tilde{h}}{l^2}\right) \sim \sigma\left(\frac{\tilde{h}}{R_{\mathrm{e}} h_{\mathrm{o}}}\right) \tag{4.20}$$

Reorganizing equation 4.20 we have,

$$\tilde{h} \sim -\frac{f(\lambda)\mu_c E_{rr} R_e^3}{\sigma h_o} \tag{4.21}$$

With this, we have determined both the unknown length scales by borrowing ideas from literature. We, now, proceed to derive a simple model to explain the presence of Ca_{cr}.

Scaling model for Ca_{cr}

The model is derived based on the argument that for separation to lead to coalescence, $\dot{\tilde{h}} > u_{rel}$. We begin with estimating the two velocity scales we seek to compare.

We know that $u_{rel} \sim E_{rr} R_e$. We differentiate equation 4.21 with respect to time to obtain an estimate for the rate of deformation of the interface, $\dot{\tilde{h}}$.

$$\dot{\tilde{h}} \sim \frac{f(\lambda)\mu_c E_{rr} R_e^3}{\sigma h_o^2} \dot{h_o} \tag{4.22}$$

$\dot{h_o}$ represents the rate of separation of the interfaces and is $\sim E_{rr} R_e$. Thus,

$$\dot{\tilde{h}} \sim \frac{f(\lambda)\mu_c E_{rr}^2 R_e^4}{\sigma h_o^2} \tag{4.23}$$

Comparing the two velocity scales, we have

$$\frac{\dot{\tilde{h}}}{u_{rel}} \sim \frac{f(\lambda)\mu_c E_{rr} R_e^3}{\sigma h_o^2} \tag{4.24}$$

We assume that $h_o \sim h_{min}$. h_o represents the thickness of the film between the droplets during the separation of the droplet interfaces. We expect it to scale with the film thickness at the end of the film drainage process. Therefore, we substitute the expression for h_{min} from equation 4.12 into equation 4.24.

$$\frac{\dot{\tilde{h}}}{u_{rel}} \sim f(\lambda)\ Ca\ R_e^2 \times \frac{128\pi R_1^4}{\lambda^2 Ca^3 (R_1+R_2)^6} \frac{1}{g(R_1,R_2)^2} (\log_e |\csc(\theta_i) - \cot(\theta_i)|)^2 \tag{4.25}$$

On simplifying, we have

$$\frac{\dot{\tilde{h}}}{u_{rel}} \sim f(\lambda)\ R_e^2 \times \frac{128\pi R_1^4}{\lambda^2 Ca^2 (R_1+R_2)^6} \frac{1}{g(R_1,R_2)^2} (\log_e |\csc(\theta_i) - \cot(\theta_i)|)^2 \tag{4.26}$$

The Ca_{cr} is determined by setting the ratio of the two velocity scales to be of order 1.

$$\frac{\dot{\tilde{h}}}{u_{rel}} \sim 1\ , \tag{4.27}$$

when $Ca = Ca_{cr}$.

$$Ca_{cr}^2 \sim \frac{128\pi f(\lambda)}{\lambda^2} \times \frac{R_e^2 R_1^4}{g(R_1,R_2)^2 (R_1+R_2)^6} \times (\log_e |\csc(\theta_i) - \cot(\theta_i)|)^2$$

$$Ca_{cr} \sim \left[\frac{20.05 f(\lambda)^{0.5}}{\lambda} \times \frac{R_e R_1^2}{g(R_1,R_2)(R_1+R_2)^3} \times (\log_e |\csc(\theta_i) - \cot(\theta_i)|) \right] \tag{4.28}$$

In our experiments, $R_1 \sim 150\ \mu m$ and $R_2 \sim 75\ \mu m$. Therefore, g(R_1,R_2) = 0.321 and R_e= 50 μm.

$$Ca_{\mathrm{cr}} \sim \left[\frac{6.16f(\lambda)^{0.5}}{\lambda} \times (\log_e |\csc(\theta_i) - \cot(\theta_i)|)\right] \tag{4.29}$$

For $Ca > Ca_{\mathrm{cr}}$ or equivalently $\frac{\dot{\hbar}}{u_{\mathrm{rel}}} < 1$, separation of droplets does not lead to coalescence.

4.2.4. Experimental data

Introduction to the experiments

In our experiments, as discussed in section 4.2.2, it was observed that if the droplets coalesce, they do so in quadrant 1 or quadrant 4 (see figure 4.5), where the droplets tend to separate away from each other. As a result, it was concluded that the observed coalescence phenomena are triggered by the separation of the droplets. The parameters measured in each experiment are the impact angle, θ_{i}, and the time taken for coalescence from the moment of impact, t. Firstly, we check if there is any dependency between the two.

The time taken for droplets to coalesce is plotted against the impact angle (see figure 4.9). It is important to note here that the measured time is defined as the duration between the time of impact to the time of coalescence. In figure 4.9a, the dimensional time is directly plotted against θ_{i}. While it appears like a trend may be deduced between the two parameters, the scatter in the data is quite large. This is because there is a large variation in the droplet size and the flow rate of the oil phase between the data points. In figure 4.9b, the measured time, t, is non-dimensionalized by a parameter, t_{N}, such that

$$t_{\mathrm{N}} = \int_{\theta_i=150}^{\theta_i=120} \frac{(R_1 + R_2)}{u_\theta|_{R_1+R_2}} \partial\theta \tag{4.30}$$

t_{N} represents the time taken by a particle that follows the flow to travel from an angle of $\theta_i = 150$ to $\theta_i = 120$ when it is at a distance of $r = R_1 + R_2$ from the origin. We suspect that the measured experimental time is largely contributed by the time taken for the motion of the droplet from quadrant 2 or quadrant 3 to quadrant 1 or quadrant 4, respectively. Therefore, by normalizing the measured time with the advection time scale, we expect a collapse of the data plotted in figure 4.9a. Although there is still a slight scattering of the data points especially at large θ_{i}, there is a significant collapse in the data, and a definite trend is observed between $\frac{t}{t_{\mathrm{N}}}$ against θ_i, thereby confirming our suspicion.

One additional investigation is performed to distinguish if the observed trend in figure 4.9b is merely a consequence of the droplets being advected in the flow or if the data reveals information related to the process of separation-driven coalescence. We estimate the time taken for the motion of the droplet from its impact position corresponding to θ_i to θ_{c}, where θ_{c} is the angle of coalescence as,

$$t_{\mathrm{adv}} = \int_{\theta_i}^{\theta_c} \frac{(R_1 + R_2)}{u_\theta|_{R_1+R_2}} \partial\theta \tag{4.31}$$

We compare the time calculated through this expression, t_{adv}, to the measured time in the experiments. To proceed with this investigation, we need knowledge of θ_{c}. Experimentally, no single angle of coalescence could be determined and the droplets coalesce between $\theta_{\mathrm{c}} = 90$ and $\theta_{\mathrm{c}} = 0$. Therefore, we choose three different values of θ_{c}, namely 90°, 60°, and 30°, to gather a rough idea of the various advection times. The estimated duration, computed through equation 4.31, is plotted as the dashed lines in figure 4.9b. It can be seen that the estimated time matches the experimental data in trend and by scaling the theoretical time by a factor of 0.33, most of the experimental data points can be explained

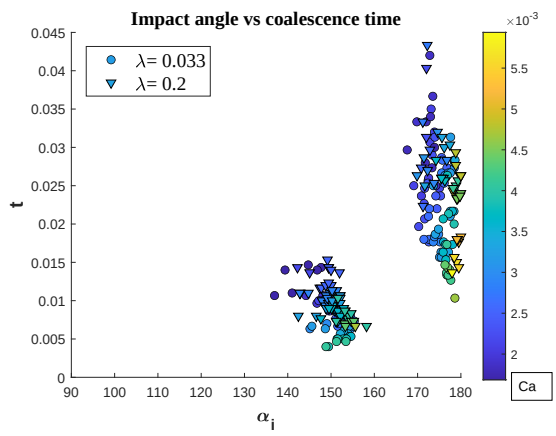

(a) Plot showing the variation of the measured time against the impact angle

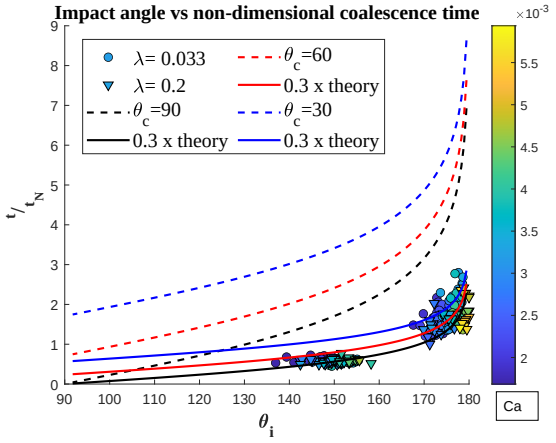

(b) Plot showing the variation of the non-dimensional measured time against the impact angle.

Figure 4.9: Plots showing a trend between the time and the impact angle, θ_i. The duration measured is from the moment of impact to the moment of coalescence.

by one of these curves. Moreover, we see that at higher θ_{i}, the range of coalescence angles is larger. From this, we can also conclude that the slight scatter in the non-dimensional time plotted in figure 4.9b is a consequence of the uncertainty in θ_{c}.

The final observation we make over plot 4.9b is that the data points correspond to a larger range of Ca at θ_{i} close to 180° while the range of Ca is reduced at θ_{i} nearing 90°, suggesting a dependency of Ca_{cr} on the θ_{i}. This is in line with the predictions of the model developed in section 4.2.3.

Interestingly, we see that the time predicted theoretically is 3 times larger than the time measured in the experiments, meaning, the droplets travel 3 times faster under experimental conditions than under the assumption that they follow the flow. This could be partly explained by recognizing that the actual flow in the device is the classic fluid mechanics problem of flow past a confined cylinder while the kinematic model derived in equation 4.31 is based on the flow past an unconfined cylinder. The blockage ratio, i.e, the ratio of the area of the channel cross-section to the cross-sectional area blocked by the droplet, is nearly 2. As a result, the local free stream velocity of the oil is larger than the free stream velocity far away from the interrogation area by a factor of 2.

In summary, the time scales of the coalescence process itself could not be resolved through the current measurement technique and a non-trivial relationship between the measured time for coalescence and the impact angle could not be found. In other words, the frame rate used in the acquisition of images, namely 3000 fps, was insufficient to resolve the time scales relevant to separation-driven coalescence. Secondly, the overlap between the experimentally measured time and the kinematic model developed in equation 4.31 suggests that the flow field around the trapped droplet can be qualitatively represented using potential flow theory. With these conclusions, we shift our focus towards investigating the Ca_{cr}.

Experimental estimates of Ca_{cr}

In this section, the experimentally measured Ca_{cr} are reported. Firstly, the manner by which the Ca_{cr} is computed from the experiments is explained. It is, then, compared against the model developed in section 4.2.3.

As mentioned previously, for an experimental set with fixed λ and fixed θ_{i}, the only parameter varied while experimenting is the Ca. The Ca is changed by slowly increasing the flow rate of oil flowing through the channels. Each experimental set could be performed only beyond a certain Ca corresponding to

the minimum flow rates at which droplets can be dragged out of the rail. This is a limitation of the experimental setup. While this limitation will always render a lower limit to the Ca achievable with the experimental set-up, the limit itself can be lowered further by making the rails less deep closer to the end of the rail. To do this, we need to use micro-fabrication methods of higher resolution. The minimum Ca at which the experiments could be carried out with the current experimental device is around 0.002.

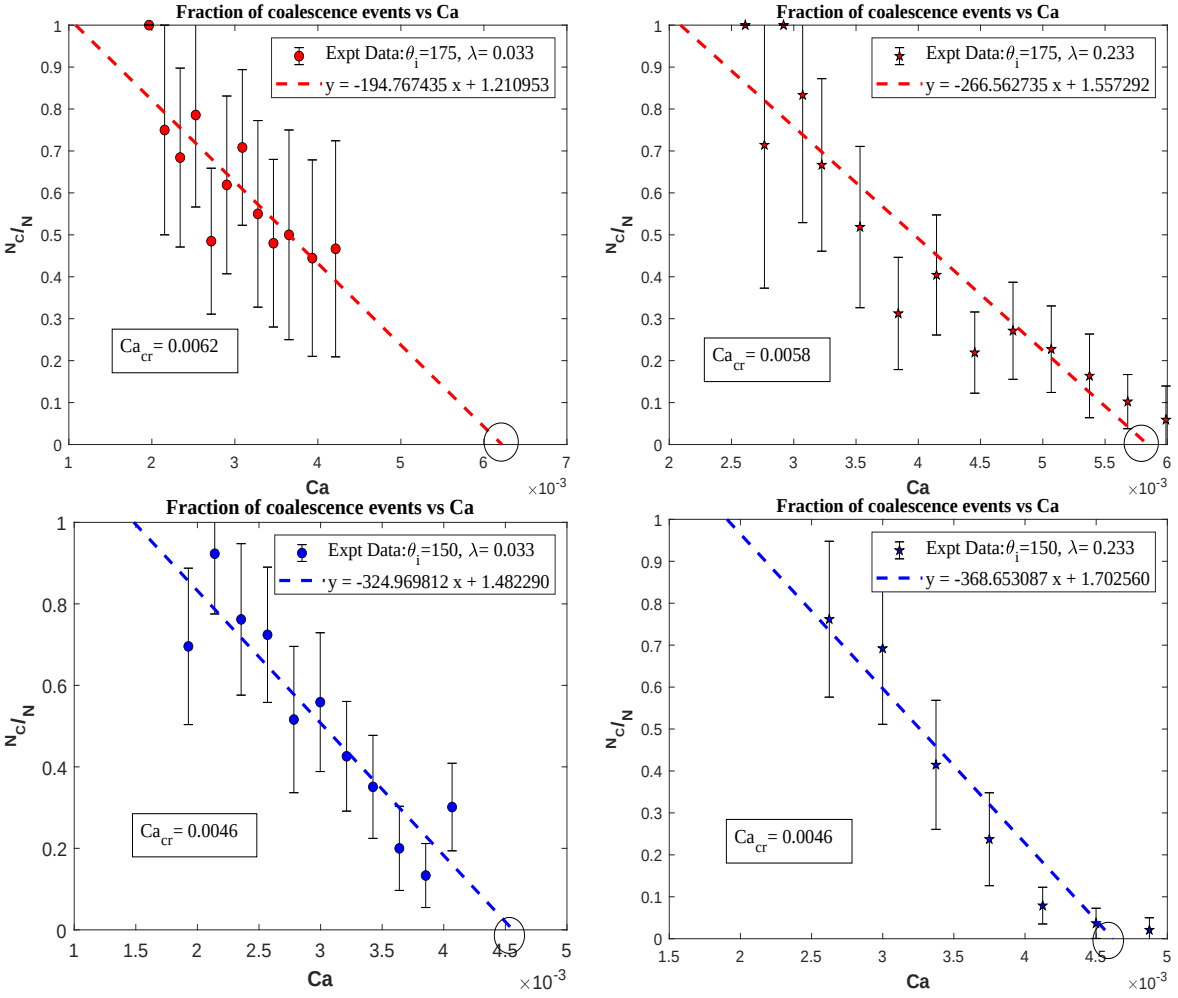

Figure 4.10: Plots showing the fraction of coalescence events observed at each Ca for four different experimental sets.

While the objectives of the study were to investigate the effect of the system parameters on Ca_{cr}, we first report the existence of a Ca_{cr} observable in the experimental set up as our first result. This result is validated by previous studies in microfluidic devices (Gunes et al., 2013) and thin films (Chatzigiannakis et al., 2020) that also report the presence of a Ca_{cr} beyond which separation does not lead to coalescence. Secondly, we report that the transition from a coalescence-non coalescence regime is not sharp, but is gradual. Consequently, the fraction of coalescence events at different Ca was measured and has been plotted in figure 4.10. By assuming that the binomial distribution may be approximated as a normal distribution, the standard error on the fraction of coalescence events was computed. The fraction of coalescence events declines with Ca and progresses close to zero. By fitting a line through the data points and extrapolating the line to a fraction corresponding to zero coalescence events, the Ca_{cr} is experimentally determined. In other words, the Ca_{cr} is computed as the x-intercept of the fitted line and is represented by the circles in figure 4.10. The error in the estimation of the Ca_{cr} is obtained

within a 95 % confidence interval (see appendix B). At low impact angles, from experiments in microfluidic devices, the Ca_{cr} was estimated to be 0.014 (Gunes et al., 2013) for a system of $\lambda = 0.01$. We arrive with a comparable estimate of $Ca_{\mathrm{cr}} \sim 0.0062$ for $\lambda = 0.033$ and $Ca_{\mathrm{cr}} \sim 0.0058$ for $\lambda = 0.2$ (see figure 4.10).

From the estimates of the Ca_{cr} between experimental data sets of different θ_{i} plotted in figure 4.11, it appears that the Ca_{cr} decreases with decreasing θ_{i}. For the lowest θ_{i} tested (θ_{i}=120°), it was not possible to estimate the Ca_{cr} using the current device as the droplets failed to coalesce on separation at the minimum attainable Ca (Ca $\sim$ 0.002). Thus, in the figure 4.11, Ca= 0.002 is marked as the upper boundary of the Ca_{cr} at $\theta_{\mathrm{i}} = 120$, estimated from the current experiment. At this moment, it is difficult to make a conclusion regarding the dependency of Ca_{cr} on θ_{i} due to the estimated uncertainty in the prediction of Ca_{cr}, marked in figure 4.11. However, we argue that the possible dependency of the Ca_{cr} on θ_{i} that we witness in our experiments arises due to the available time for film drainage before droplet separation. As can be easily noticed from figure 4.1, the available time for film drainage is compromised as θ_{i} approaches 90°, leading to a thicker film at the onset of droplet separation. The effect of a thicker film is not only to increase the absolute distance between the two droplets before separation, but also to reduce the absolute magnitude of the suction pressure in the film (see equation 4.17). The effect of both these consequences is to suppress coalescence. Within the expected uncertainty in the estimation of Ca_{cr}, no dependency could be found between the Ca_{cr} and λ experimentally (see 4.10), despite the λ of the two systems being one order of magnitude apart.

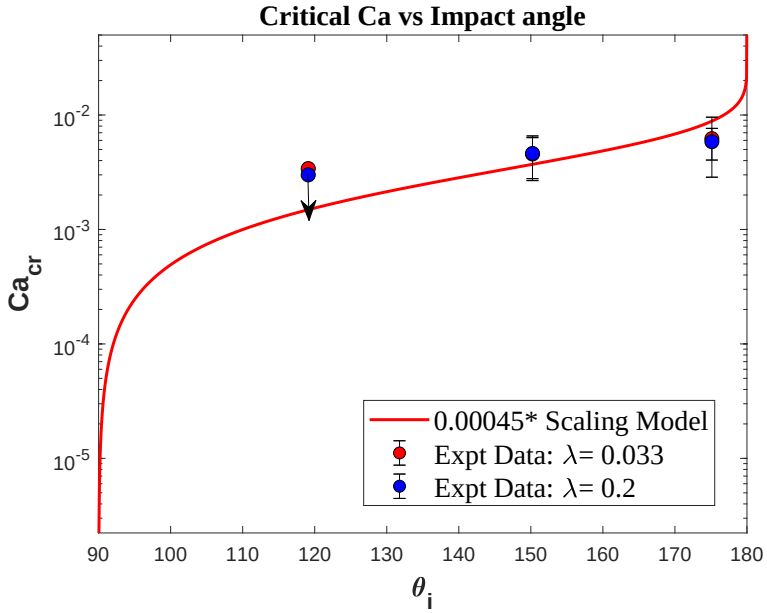

Figure 4.11: Plot showing the variation of the Ca_{cr} with the impact angle of collision obtained from experiments. The values are compared against the model developed in section 4.2.3

The results from our experiments are now compared to the predictions of the model derived in section 4.2.3. In the model, the effect of the film drainage phase is taken into account by scaling the thickness of the film between the droplets just before separation, h_{o}, with the estimated film thickness, h_{min}, at the end of the drainage process, i.e, at θ = 90°. By comparing the values for Ca_{cr} obtained experimentally against the model (see figure 4.11), we see that the model fits the data, within the experimental uncertainty limits, qualitatively. However, the model predicts values that are four orders of magnitude larger than what is experimentally observed. The origin of this scaling factor is currently unknown to

the author. Increasing contact times between droplets before separation was found to increase the Ca_{cr} (Gunes et al., 2013) although a qualitative or quantitative relationship between the two was not presented. The experimentally obtained dependency of Ca_{cr} on λ is also in apparent disagreement with the scaling model that predicts $Ca_{\mathrm{cr}} \sim \lambda^{-1}$, although it cannot be said for certain since the function f(λ) is unknown at the moment. In the case that f(λ) $\sim \lambda^2$, the model would also predict only a weak dependency of the Ca_{cr} over λ. In line with this possibility, as stated earlier, the Ca_{cr} obtained by Gunes et al., 2013 in their study of a system of λ = 0.01 falls fairly close to the estimates in this study over systems of λ that are considerably larger than λ = 0.01.

In summary, we first report the presence of Ca_{cr} observed in our experiments such that for $Ca > Ca_{\mathrm{Cr}}$, separation of droplets does not drive coalescence. On investigating the dependency of the Ca_{cr} on the impact angle, θ_i, we see a decrease in Ca_{cr} as θ_i was decreased. However, we note that the estimated uncertainty in the experimentally determined Ca_{cr} is quite large which makes it difficult to derive any conclusions with the currently available information. In any case, we argue that the apparent dependency of Ca_{cr} over θ_i is, in fact, a consequence of the time allowed for the drainage of the film to proceed before separation. Finally, we observe no dependency of the Ca_{cr} over λ. The model developed in section 4.2.3 also predicts the presence of a Ca_{cr} and this was confirmed in the experiments. The model explains the experimental data for the dependency of Ca_{cr} over θ_{i} qualitatively. The extent of agreement between the model and experimental results adds further evidence to the hypothesis that separation of two droplets leads to coalescence due to local bulging of the interfaces in response to the suction pressure in the film. However, while the agreement indicates the right direction, further research is required to evaluate the extent to which the model grasps the physics of the process.

5

Conclusions

The objective of this thesis was to develop a microfluidic device in which we can observe the coalescence of two droplets. We proposed to develop this device by taking advantage of surface energy wells. By using a combination of anchors and rails to trap and guide droplets, we intended to realize repeatable and controllable collisions in the device. Apart from serving as a proof-of-concept, we sought to use the developed device in the study of coalescence of two droplets. A specific mechanism of coalescence termed in literature as 'separation-driven coalescence' was the problem of interest in this thesis. We sought to understand the presence of a critical limit for separation-driven coalescence in terms of a non-dimensional parameter, Ca. The effect of the system parameters on the Ca_{cr} was studied.

A microfluidic device, consisting of anchors and rails, was designed and fabricated through rapid prototyping. The dimensions of the functioning device are presented and justified in section 3.5. The designed device was tested and proved to deliver better control over droplet collisions with high repeatability in comparison to a device without rails (refer section 4.1). The control over the impact angle in the device is limited by the resolution of the fabrication method. Currently, the rail is 200 μm in width and is limited by the lowest dimension realizable in the XY plane with the chosen fabrication method. Therefore, the variation in the impact position of the droplets is up to 200 μm. By using a fabrication method of higher resolution, the width of the rail can be reduced and the impact position of the droplets can be controlled with more accuracy. However, we conclude that using surface energy wells, specifically a combination of rails and anchors, can help in realizing repeatable and controllable droplet collisions.

The proposed design was used as a part of the experimental setup for the systematic study of separation-driven droplet coalescence. Three devices were fabricated differing in the position of the rail such that in each device, the rails facilitated a different impact angle of collision. A total of two systems were tested - a water-oil system ($\lambda = 0.033$) and a glycerol-water mixture-oil system ($\lambda = 0.2$). We first acknowledge the presence of Ca_{cr} beyond which separation between droplets does not lead to coalescence. Ca_{cr} was determined for each experimental set consisting of a specific θ_{i} and specific λ. We found that the Ca_{cr} decreases with decreasing θ_{i}. A weak dependency of Ca_{cr} on λ was observed in the experiments. However, we note that the uncertainty in the experimentally determined values of Ca_{cr} is large.

A model was developed to explain the presence of a Ca_{cr} based on the hypothesis that separating droplets coalesce due to the suction pressure developed in the intervening film between separating interfaces (Leal, 2004). The model succeeds in predicting the presence of a Ca_{cr} for separation-driven coalescence. Further, the model captures the effect of θ_i on the Ca_{cr} qualitatively. Based on this agreement, we conclude that the time available for the drainage of the film between the two droplets before separation plays a role in determining the Ca_{cr}. A thinner film on the onset of separation increases the Ca_{cr} since it increases the velocity scale for deformation of the interface. The observed concurrence between the model and experimental values suggests that the hypothesis adopted in the model explains the mechanism of separation-driven coalescence. However, the model predicts values for the Ca_{cr} that are four orders of magnitude larger than found experimentally. The model is also unable to predict the effects of λ on the Ca_{cr}.

In this study, we have established a framework for studying micro-droplet coalescence and specifically-separation-driven coalescence. The device developed in the study is a first step towards building a robust experimental set-up for droplet coalescence studies. While the underlying concept of its design can be adopted, better fabrication methods must be used to further this research. Secondly, a framework for experimentally determining the Ca_{cr} has been established. We also derived a model to explain the experimental results. Due to the limitations of the setup and the paucity of time, enough experimental data could not be collected. As a result, a rigorous analysis of the phenomena and evaluation of the model could not be carried out. Hence, we did not arrive at conclusive results regarding the dependency of θ_i and λ on Ca_{cr}. By working with the framework established in this thesis, better insights into the fascinating phenomena of droplet coalescence can be gained on pursuing this research. A few suggestions that can improve this study are discussed in the next section.

5.1. Recommendations for future work

Firstly, the recommendations for the design and fabrication of this device are discussed. The use of rails and anchors has significantly improved the control over droplet collisions attainable in microfluidic devices, despite the low resolution of the fabrication method used in this study. The purpose of this study was to assess the potential of using surface energy wells in coalescence studies and the results we have obtained motivate us to develop a scaled-down device by shifting to a fabrication method of higher resolution. This can provide us better control and selectivity over the impact angle of collision. A suggested technique is to fabricate silicon wafer molds instead of 3-D printed molds. Secondly, in the current device, the only parameters that can be tuned by the experimentalist after choosing a device (in terms of positioning of the rail) and the two-phase system are the input flow rates of the two phases. By changing the flow rate of the continuous phase (oil), we can study the problem at different Ca. The current design is such that any change to the flow rate of the phases made to study its effect on the coalescence process (at the interrogation area) cannot be done without affecting the droplet generation process (at the T-junction). This is quite inconvenient since, apart from affecting the stability of the droplet generation at the T-junction, the size of the droplets and the frequency of droplet generation are also continuously changing as we run the experiment under a gradually changing flow rate of oil (see appendix A). To overcome this, we can improve the design of the device by including additional channels that connect to the main channel after the T-junction and before the interrogation area. Additional syringe pumps can be used to push oil through these channels. With this design, we can have independent control over the flow rates realizable at the interrogation area without influencing the droplet generation process at the T-junction. However, it comes at the cost of complicating the

design and operation of the device.

"It is only by a patient separation of different physical regimes that one may hope to reach the physical laws".- de Gennes (De Gennes, 1985). In this vein, we discuss further experiments that can be performed using the developed device to emerge onto a unified understanding of the coalescence process. Firstly, experiments can be performed with the existing set-up to determine more accurate estimates of the Ca_{cr}. Secondly, having fabricated a scaled-down device, we must focus on sampling more impact angles between $\theta_{\mathrm{i}} = 180 - 170$ and $\theta_i = 120 - 90$ where the model predicts sharp changes in the Ca_{cr} with θ_{i} (see figure 4.11). Testing these impact angles will help us arrive at more conclusive results regarding the effects of the film drainage phase in separation-driven coalescence. Finally, the transition from approach driven-coalescence to separation-driven coalescence can also be investigated with a scaled-down device.

Finally, we present some suggestions that can reduce the approximations made while analyzing the data from experiments. As mentioned in the introduction to chapter 4, the trapped droplet is approximated as circular droplets of radius equal to the radius of the anchor. The flow field around the droplet is assumed to be represented by the ideal flow around a cylinder of radius R_1. A better approximation of the flow field may be obtained by accounting for the real shape of the trapped droplet by using conformal mapping. Secondly, in this study, we use the expected flow field around an unconfined cylinder to represent the flow around the trapped droplet which in reality is a confined object. As a result, the forces and relative velocities (Ca) estimated experimentally may be underestimated. It is possible that the underestimation of the Ca partly contributes to the discrepancy in the magnitude of the Ca_{cr} between the model and the experiments. A better estimate of the flow field may be obtained by treating the trapped droplet as a confined object. To do this, a Particle Image Velocimetry (PIV) study could be performed to experimentally estimate the flow field around the trapped droplet. However, introducing particles in a coalescence study can affect the behaviour of the interfaces (Gafonova and Yarranton, 2001, Sullivan and Kilpatrick, 2002). Hence, a PIV study should only be done to determine the flow field around the trapped droplet and not to gather any information on the coalescence process. Finally, in the development of the scaling model in section 4.2.3, we couple the film drainage process to the model through the introduction of the film thickness,h_{min}. The parallel-disk model for film drainage was developed for two isolated droplets that collide with each other. In our experiments, the droplets are pancake-shaped. With such a configuration, it is possible that the drainage process is altered and proceeds at a slower rate due to the confinement from the top and bottom walls of the channel. We can correct this by deriving a drainage rate for confined droplets such that the drainage along the height of the channel is neglected.

A

Droplet generation in T-junction

In this thesis, droplets were generated at the T-junction. The size of the droplets against the Ca defined at the T-junction is plotted in figure A.1. The Ca is defined as,

$$Ca = \frac{\mu_c u_T}{\sigma} \tag{A.1}$$

where u_T is the velocity of the oil phase computed at the T-junction. In this section, we make observations regarding the droplet generation process in the microfluidic device.

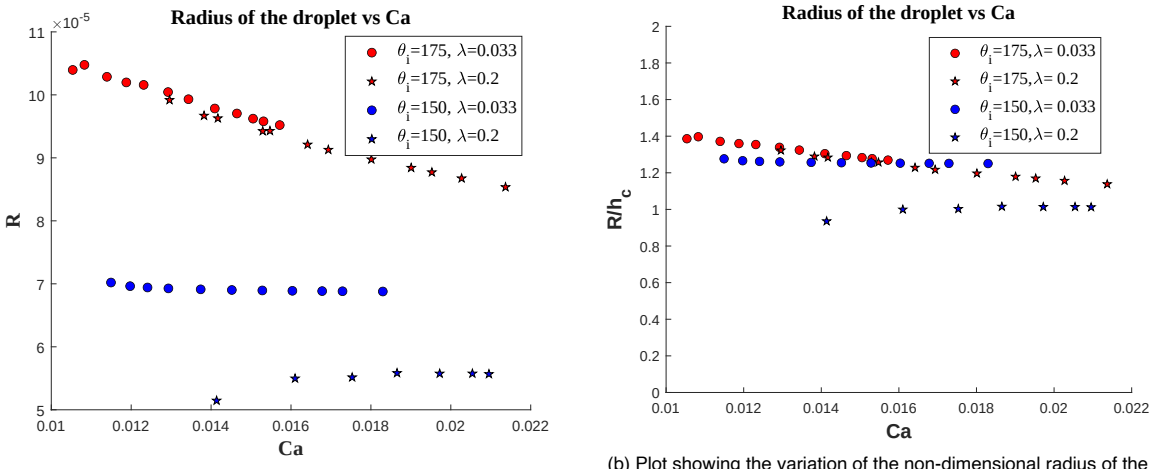

(a) Plot showing the variation of the radius of the droplet with the Ca

(b) Plot showing the variation of the non-dimensional radius of the droplet with the Ca

Figure A.1: The measured radius of the droplets generated at the T junction

In figure A.1a, the radius of the droplet generated at the T-junction, R, is plotted against Ca. Firstly, we see a very slight dependency of R with Ca within each experimental data set. The Ca at the T-junction changes as a consequence of the change in the flow rate of the oil phase. Experimentally, we increase the flow rate of the oil phase to change the Ca at the interrogation area. Since the T-junction and the interrogation area are coupled in the device, it is not possible to vary one without affecting the other. This is a limitation of the device since ideally we would like to study the effects of the Ca on the coalescence phenomenon without changing the size of the droplets. Secondly, when we compare

the R values obtained from different data sets, we see considerable differences. This difference in R across experimental data sets is quite striking. For example, in figure A.1a droplet sizes vary between data sets of θ_i = 175°and θ_i = 150°. We note here that between both these devices, the only difference in the design is the position of the rail and the T-junction is designed to be the same. To investigate this, we made cross-sections of the T-junction in both the devices to check if the cross-sectional area of the T-junction was the same. We found that in the device where the θ_i= 175°, the height of the channel, h_c was 75 μm, as per design. In the device where the θ_i= 150°, h_c was around 55 μm. This discrepancy is a consequence of the errors made in the fabrication of the mold. We reiterate that we do not expect this difference to originate due to the positioning of the rail. In figure A.1b, we non-dimensionalize R by h_c and we see a better collapse of the data.

The result from the droplet generation process is further evidence that better fabrication methods must be used in the further course of this research. We remark that, in this study, the actual size of the droplet is always taken into consideration while computing parameters experimentally.

B

Error in estimation of Ca_{cr}

In this chapter, the manner in which the error in the experimentally deduced Ca_{cr} was determined is presented. As mentioned previously, the Ca_{cr} was estimated as the x-intercept of the fitted line in figure 4.10. Therefore, by fitting a line through the data points, we obtained an equation for the line as

$$n_{\mathrm{c}} = m\ Ca + c \tag{B.1}$$

where n_{c} is the fraction of coalescence events, m is the slope of the line, and c is a constant. To compute the x- intercept, we say the n_{c} (Ca= Ca_{cr}) = 0. Therefore, we arrive at the Ca_{cr} as,

$$Ca_{\mathrm{cr}} = f(m,c) = \frac{-c}{m} \tag{B.2}$$

where Ca_{cr} is represented as $f(m,c)$.The errors in the estimation of m and c are known from the results of the fitting function. We represent the error in m as Δe_{m}, the error in c as Δe_{c}, and the error in Ca_{cr} as Δe_{i}. Then, Δe_{i} is obtained as,

$$\Delta e_{\mathrm{i}} = \left[\left(\frac{\partial f(m,c)}{\partial m}\Delta e_{\mathrm{m}}\right)^2 + \left(\frac{\partial f(m,c)}{\partial c}\Delta e_{\mathrm{c}}\right)^2\right]^{1/2} \tag{B.3}$$

$$\Delta e_{\mathrm{i}} = \left[\left(\frac{c}{m^2}\Delta e_{\mathrm{m}}\right)^2 + \left(\frac{-1}{m}\Delta e_{\mathrm{c}}\right)^2\right]^{1/2} \tag{B.4}$$

Bibliography

Aarts, D. G., Lekkerkerker, H. N., Guo, H., Wegdam, G. H., & Bonn, D. (2005). Hydrodynamics of droplet coalescence. *Physical review letters*, *95*(16), 164503.

Abbyad, P., Dangla, R., Alexandrou, A., & Baroud, C. N. (2011). Rails and anchors: Guiding and trapping droplet microreactors in two dimensions. *Lab on a Chip*, *11*(5), 813–821.

Anna, S. L., Bontoux, N., & Stone, H. A. (2003). Formation of dispersions using "flow focusing" in microchannels. *Applied physics letters*, *82*(3), 364–366.

Baldessari, F., & Leal, L. G. (2006). Effect of overall drop deformation on flow-induced coalescence at low capillary numbers. *Physics of fluids*, *18*(1), 013602.

Beatus, T., Bar-Ziv, R. H., & Tlusty, T. (2012). The physics of 2d microfluidic droplet ensembles. *Physics reports*, *516*(3), 103–145.

Bremond, N., Thiam, A. R., & Bibette, J. (2008). Decompressing emulsion droplets favors coalescence. *Physical review letters*, *100*(2), 024501.

Brunaugh, A. D., Smyth, H. D. C., & Williams III, R. O. (2019). Disperse systems: Suspensions. *Essential pharmaceutics* (pp. 91–110). Springer International Publishing. https://doi.org/10.1007/978-3-030-31745-4_6

Chatzigiannakis, E., Veenstra, P., Ten Bosch, D., & Vermant, J. (2020). Mimicking coalescence using a pressure-controlled dynamic thin film balance. *Soft Matter*, *16*(41), 9410–9422.

Chesters, A. (1991). Modelling of coalescence processes in fluid-liquid dispersions: A review of current understanding. *Chemical engineering research and design*, *69*(A4), 259–270.

Christopher, G., Bergstein, J., End, N., Poon, M., Nguyen, C., & Anna, S. L. (2009). Coalescence and splitting of confined droplets at microfluidic junctions. *Lab on a Chip*, *9*(8), 1102–1109.

Dangla, R., Lee, S., & Baroud, C. N. (2011). Trapping microfluidic drops in wells of surface energy. *Physical review letters*, *107*(12), 124501.

De Gennes, P.-G. (1985). Wetting: Statics and dynamics. *Reviews of modern physics*, *57*(3), 827.

De Menech, M., Garstecki, P., Jousse, F., & Stone, H. A. (2008). Transition from squeezing to dripping in a microfluidic t-shaped junction. *journal of fluid mechanics*, *595*, 141–161.

Duffy, D. C., McDonald, J. C., Schueller, O. J., & Whitesides, G. M. (1998). Rapid prototyping of microfluidic systems in poly (dimethylsiloxane). *Analytical chemistry*, *70*(23), 4974–4984.

Fidalgo, L. M., Abell, C., & Huck, W. T. (2007). Surface-induced droplet fusion in microfluidic devices. *Lab on a Chip*, *7*(8), 984–986.

Frenz, L., Blank, K., Brouzes, E., & Griffiths, A. D. (2009). Reliable microfluidic on-chip incubation of droplets in delay-lines. *Lab on a Chip*, *9*(10), 1344–1348.

Gafonova, O. V., & Yarranton, H. W. (2001). The stabilization of water-in-hydrocarbon emulsions by asphaltenes and resins. *Journal of Colloid and Interface Science*, *241*(2), 469–478.

Glawdel, T., Elbuken, C., & Ren, C. L. (2012). Droplet formation in microfluidic t-junction generators operating in the transitional regime. i. experimental observations. *Physical Review E*, *85*(1), 016322.

Guido, S., & Simeone, M. (1998). Binary collision of drops in simple shear flow by computer-assisted video optical microscopy. *Journal of Fluid Mechanics*, *357*, 1–20.

Gunes, D. Z., Bercy, M., Watzke, B., Breton, O., & Burbidge, A. S. (2013). A study of extensional flow induced coalescence in microfluidic geometries with lateral channels. *Soft Matter*, *9*(31), 7526–7537.

Hele-Shaw, H. (1898). Experimental investigation of the motion of a thin film of viscous fluid. *British Association for the Advancement of Science Reports*, *1898*, 136–142.

Janssen, P. J., & Anderson, P. D. (2011). Modeling film drainage and coalescence of drops in a viscous fluid. *Macromolecular Materials and Engineering*, *296*(3-4), 238–248.

Joanicot, M., & Ajdari, A. (2005). Droplet control for microfluidics. *Science*, *309*(5736), 887–888.

Kamp, J., Villwock, J., & Kraume, M. (2017). Drop coalescence in technical liquid/liquid applications: A review on experimental techniques and modeling approaches. *Reviews in Chemical Engineering*, *33*(1), 1–47.

Lai, A., Bremond, N., & Stone, H. A. (2009). Separation-driven coalescence of droplets: An analytical criterion for the approach to contact. *Journal of fluid mechanics*, *632*, 97–107.

Leal, L. (2004). Flow induced coalescence of drops in a viscous fluid. *Physics of fluids*, *16*(6), 1833–1851.

Leal-Calderon, F., Schmitt, V., & Bibette, J. (2007). *Emulsion science: Basic principles*. Springer Science & Business Media.

Lederberg, J. (1954). A simple method for isolating individual microbes. *Journal of bacteriology*, *68*(2), 258.

Link, D., Anna, S. L., Weitz, D., & Stone, H. (2004). Geometrically mediated breakup of drops in microfluidic devices. *Physical review letters*, *92*(5), 054503.

McDonald, J. C., Duffy, D. C., Anderson, J. R., Chiu, D. T., Wu, H., Schueller, O. J., & Whitesides, G. M. (2000). Fabrication of microfluidic systems in poly (dimethylsiloxane). *ELECTROPHORESIS: An International Journal*, *21*(1), 27–40.

Meleson, K., Graves, S., & Mason, T. G. (2004). Formation of concentrated nanoemulsions by extreme shear. *Soft Materials*, *2*(2-3), 109–123.

Mousa, H., Agterof, W., & Mellema, J. (2001). Experimental investigation of the orthokinetic coalescence efficiency of droplets in simple shear flow. *Journal of colloid and interface science*, *240*(1), 340–348.

Posocco, P., Perazzo, A., Preziosi, V., Laurini, E., Pricl, S., & Guido, S. (2016). Interfacial tension of oil/water emulsions with mixed non-ionic surfactants: Comparison between experiments and molecular simulations. *RSC advances*, *6*(6), 4723–4729.

Reynolds, O. (1886). Iv. on the theory of lubrication and its application to mr. beauchamp tower's experiments, including an experimental determination of the viscosity of olive oil. *Philosophical transactions of the Royal Society of London*, (177), 157–234.

Shim, J.-u., Cristobal, G., Link, D. R., Thorsen, T., Jia, Y., Piattelli, K., & Fraden, S. (2007). Control and measurement of the phase behavior of aqueous solutions using microfluidics. *Journal of the American Chemical Society*, *129*(28), 8825–8835.

Sinzato, Y. Z., Dias, N. J. S., & Cunha, F. R. (2017). An experimental investigation of the interfacial tension between liquid-liquid mixtures in the presence of surfactants. *Experimental Thermal and Fluid Science*, *85*, 370–378.

Stone, H. A., Stroock, A. D., & Ajdari, A. (2004). Engineering flows in small devices: Microfluidics toward a lab-on-a-chip. *Annu. Rev. Fluid Mech.*, *36*, 381–411.

Sullivan, A. P., & Kilpatrick, P. K. (2002). The effects of inorganic solid particles on water and crude oil emulsion stability. *Industrial & engineering chemistry research*, *41*(14), 3389–3404.

Theberge, A. B., Courtois, F., Schaerli, Y., Fischlechner, M., Abell, C., Hollfelder, F., & Huck, W. T. (2010). Microdroplets in microfluidics: An evolving platform for discoveries in chemistry and biology. *Angewandte Chemie International Edition*, *49*(34), 5846–5868.

Vinckier, I., Moldenaers, P., Terracciano, A., & Grizzuti, N. (1998). Droplet size evolution during coalescence in semiconcentrated model blends. *AIChE journal*, *44*(4), 951–958.

Wang, K., Lu, Y., Yang, L., & Luo, G. (2013). Microdroplet coalescences at microchannel junctions with different collision angles. *AIChE Journal*, *59*(2), 643–649.

Whitesides, G. M. (2006). The origins and the future of microfluidics. *nature*, *442*(7101), 368–373.

Xu, S., Nie, Z., Seo, M., Lewis, P., Kumacheva, E., Stone, H. A., Garstecki, P., Weibel, D. B., Gitlin, I., & Whitesides, G. M. (2005). Generation of monodisperse particles by using microfluidics: Control over size, shape, and composition. *Angewandte Chemie*, *117*(5), 734–738.

Yiantsios, S. G., & Davis, R. H. (1990). On the buoyancy-driven motion of a drop towards a rigid surface or a deformable interface. *Journal of Fluid Mechanics*, *217*, 547–573. https://doi.org/10.1017/S0022112090000842